

Molecular Line Ratio Diagnostics Along the Radial Cut and Dusty UV-bright Clumps in a Spiral Galaxy NGC 0628

Selçuk Topal^{1,2*}

¹Van 100. Yil University, Department of Physics, Van, 65080, Turkey

²Sub-department of Astrophysics, University of Oxford, Denys Wilkinson Building, Keble Road, Oxford OX1 3RH, U.K.

Accepted . Received ; in original form

ABSTRACT

Molecular emission lines are essential tools to shed lights on many questions regarding star formation in galaxies. Multiple molecular lines are particularly useful to probe different phases of star-forming molecular clouds. In this study, we investigate the physical properties of giant molecular clouds (GMCs) using multiple lines of CO, i.e. CO(1–0, 2–1, 3–2) and ¹³CO(1–0), obtained at selected 20 positions in the disc of NGC 0628. Eleven positions were selected over the radial cut, including the centre, and remaining nine positions were selected across the southern and northern arms of the galaxy. 13 out of 20 positions are brighter at 24 μ m and ultraviolet (UV) emission and hosting significantly more H II regions compared to the rest of the positions indicating opposite characteristics. Our line ratio analysis shows that the gas gets warmer and thinner as a function of radius from the galaxy centre up to 1.7 kpc, and then the ratios start to fluctuate. Our empirical and model results suggest that the UV-bright positions have colder and thinner CO gas with higher hydrogen and CO column densities. However, the UV-dim positions have relatively warmer CO gas with lower densities bathed in GMCs surrounded by less number of H II regions. Analysis of multi-wavelength infrared and UV data indicates that the UV-bright positions have higher star formation efficiency than that of the UV-dim positions.

Key words: galaxies: spiral - galaxies: ISM - ISM: molecules - ISM: H II regions - ISM: dust

1 INTRODUCTION

The interstellar medium (ISM) of galaxies are the sites for stars to be born and die, providing fingerprints of past and current star formation activities. One of the ways to track these fingerprints down is to study molecular emission lines as they are results of different physical conditions in molecular clouds, e.g. different temperature, density, and opacity. Molecules are necessary coolants for the gas clouds, helping the clouds to collapse and form stars. Molecules, therefore, have a vital role in better understanding the physics of the gas leading stars to be born and shaping the ISM of a galaxy.

The Universe consists of many types of galaxies from giant ellipticals to spirals; each has a different amount of molecular gas and shows different levels of star formation activity. Spiral galaxies, like the subject of this study NGC 0628, have a substantial amount of molecular gas allowing us to probe the nature of star-forming gas in greater details. Carbon monoxide (CO) is the second most abundant molecule in the ISM after hydrogen molecule (H₂). At high densities, where stars are born, hydrogen tends to be molecular, but it is tough to observe directly due to its quantum structure.

We, therefore, use proxies instead, such as CO, a well-known proxy to probe the physical properties of molecular gas indirectly. Since molecular gas is strongly correlated with star formation (Dobbs et al. 2014 and references therein), studying the properties of the gas has an unignorable potential to answer many outstanding questions regarding star formation processes in galaxies and evolution of galaxies at large.

Effects of the ultraviolet (UV) radiation to giant molecular clouds (GMCs) are either destructive or advantageous in terms of star formation (e.g. Elmegreen & Lada 1977; Deharveng et al. 2010; Bisbas et al. 2011; Medina et al. 2014; Kim et al. 2018), but the UV radiation feedback overall has negative effects (e.g. McKee & Ostriker 2007). UV radiation field also plays an essential role in regulating the CO abundances (van Dishoeck & Black 1988). NGC 0628 has been reported to contain as many as 376 H II complexes, one of the largest numbers in the nearby Universe (Fathi et al. 2007). H II regions are regions of photoionized gas created by ionising photons coming from O- and B-type stars, the source of UV radiation in the ISM. Photoionization is thought to be the primary cause of destruction for GMCs (e.g. Whitworth 1979; Matzner 2002; Krumholz et al. 2006) and feedbacks from supernovae, and protostellar outflows are thought to be negligible com-

* E-mail: selcuktopal@yyu.edu.tr

Table 1. General properties of NGC 0628.

Galaxy	Property	Value	Reference
NGC 0628	Type	SA(s)c	a
	RA (J2000)	1 ^h 36 ^m 41.7 ^s	a
	Dec (J2000)	15 ^d 47 ^m 01 ^s	a
	V_{\odot} (km s ⁻¹)	657	a
	Major diameter	10'5	a
	Minor diameter	9'5	a
	$SFR_{H\alpha}$ (M_{\odot} yr ⁻¹)	4.0	b
	$\log(M_{H_2}/M_{\odot})$	9.49	b
	Distance (Mpc)	7.3	c
	Position angle	25°	d
	Inclination	19.8°	d

References: ^a Nasa/Ipac Extragalactic Database (NED); ^b Kennicutt et al. 2003; ^c Karachentsev et al. 2004; ^d Makarov et al. 2014.

pared to H II regions (e.g. Krumholz et al. 2006; McKee & Ostriker 2007). While less massive GMCs ($10^4 - 10^5 M_{\odot}$) with lower densities are weaker against the feedback from H II regions, denser and more massive clouds ($> 10^6 M_{\odot}$) with larger escape velocities mostly remain dynamically unaffected by ionizing feedback (e.g. Dale et al. 2012, 2013). H II regions, as an essential energy injection source for GMCs (e.g. Matzner 2002), therefore, have a vital role in the fate of molecular gas and ultimately in star formation.

NGC 0628 (M74) is a face-on nearby spiral galaxy (7.3 Mpc; Karachentsev et al. 2004) and is well studied in both H α and far-ultraviolet (FUV) emission (Adler et al. 1999; Herbert-Fort et al. 2010), both indicating intense star formation activity in the arms. In total, we observed 20 selected positions throughout the disc of NGC 0628 in ¹²CO(1–0) and ¹³CO(1–0) lines. The positions consist of 9 positions in the arms brighter in the UV and 11 positions over the SE-NW cut, including the centre (see Figure 1). The UV-bright positions are also brighter at 24 μ m and filled with many H II regions compared to the positions located over the SE-NW cut (see Figure 1). Using our new observations and additional data of ¹²CO(2–1) and ¹²CO(3–2) from the literature, the goals of our study are: i) to increase our understanding of the star formation processes in external spiral galaxies, in particular in spiral arms; ii) to determine for the first time the properties of the molecular gas in the arms of this particular galaxy, this by using multiple lines of CO and radiative transfer modelling; iii) to probe differences in star formation activity between the spiral arms and the centre of the galaxy (and other galaxies); iv) to better understand the effects of young massive stars (hinted by intense UV radiation and H II regions) and dust to surrounding molecular gas and finally v) to study radial variations in physical conditions of the gas over the disc.

The paper is organised as follows. Section 2 describes the observations and data reduction, while § 3 presents imaging and analysis. The results and discussions are presented in § 4, and we finally conclude briefly in § 5.

2 OBSERVATIONS AND DATA REDUCTION

2.1 Observation

We have acquired new single-dish observations of CO lines in the disc of NGC 0628 (see Table 2). We defined 9 positions along the northern and southern arms of the galaxy where the FUV emission shows a peak in Galaxy Evolution Explorer Survey (GALEX) map

(Gil de Paz et al. 2007). Additionally, together with a central pointing, 11 positions over the SE-NW cut were observed (see Figure 1).

The CO(1–0) and ¹³CO(1–0) observations were carried out using the IRAM 30m telescope. The telescope is equipped with the Eight MIXer Receiver (EMIR) and a backend FTS200 providing 200 kHz frequency resolution corresponding to a velocity resolution of about 0.5 kms⁻¹ for the observing frequency of 110.201 GHz. We estimated the sensitivity level for the observation for average conditions (7.0 mm of pwv, $T_{\text{sys}} = 168.8$ K (TA^*) mean per pixel). Before applying further analysis, we binned the spectra to a velocity resolution of 5 kms⁻¹. CO(1–0) was detected (i.e. $S/N > 3\sigma$, where $\sigma = 13$ mK) in all 20 positions, while ¹³CO(1–0) was detected in 15 positions ($\sigma = 5.2$ mK). The beam size of CO(1–0) and ¹³CO(1–0) at IRAM 30m telescope is about 22'' corresponding to a linear size of 778 pc at the distance of 7.3 Mpc for NGC 0628 (Karachentsev et al. 2004), allowing us to study the physical conditions of the gas at sub-kpc resolution. The spatial coverage of the observations is shown in Figure 1, overlaid on an optical image of the galaxy (Sloan Digitized Sky Survey, SDSS).

2.2 Literature CO Data

The CO(2–1) data were taken from the HERA CO Line Extragalactic Survey (HERACLES; Leroy et al. 2009), while the data for CO(3–2) were taken from the James Clerk Maxwell Telescope (JCMT) Nearby Galaxies Legacy Survey (NGLS; Warren et al. 2010). Noise in the CO(2–1) and CO(3–2) data cubes are 22 mK and 15.8 mK, respectively (see Table 2). For more details on the observational parameters, please see the related papers.

All in all, together with the literature data, there are four lines detected at 13 out of the 20 positions and three lines at 4 positions (i.e. either ¹³CO(1–0) or CO(3–2) were not detected at those positions) and finally two lines detected at the remaining 3 positions (i.e. only CO(1–0) and CO(2–1) emission were detected).

2.3 Data Reduction

Our IRAM 30m data were reduced using the Continuum and Line Analysis Single-Dish Software (CLASS) software package in the Grenoble Image and Line Analysis System (GILDAS). A baseline fit (polynomial of order 0 or 1) was removed from each scan before averaging all integrations. The antenna temperature scale (T_A^*) was then transformed to the main beam brightness temperature scale (T_{mb}) by dividing by the main beam efficiency, η_{mb} , where $\eta_{\text{mb}} = 0.83$ and 0.84 for CO(1–0) and ¹³CO(1–0) respectively. The beam efficiencies were taken from the IRAM¹. For η_{mb} values of ¹³CO(1–0) not specified there, we linearly interpolated between the two nearest values. Each spectrum was then converted to the Flexible Image Transport System (FITS) format for further analysis in the Interactive Data Language (IDL) environment.

3 IMAGING AND ANALYSIS

3.1 Emission regions and moment maps

We created moment maps, i.e. integrated intensity map (hereafter moment 0) and velocity maps (hereafter moment 1) over the disc of NGC 0628 (see Figure 2) by following the method described

¹ <http://www.iram.es/IRAMES/mainWiki/Iram30mEfficiencies>

Table 2. Main observational parameters for NGC 0628

Transition	Rest Freq. (GHz)	Obs. Date	Telescope	Beam (arcsec)	Noise* (mK)	Reference
$^{12}\text{CO}(1-0)$	115.271	JULY 2012	IRAM 30m	22	13	This study
$^{13}\text{CO}(1-0)$	110.201				5.2	
$^{12}\text{CO}(2-1)$	230.538	JAN 2007	IRAM 30m	13.4	22	Leroy et al. 2009
$^{12}\text{CO}(3-2)$	345.795	NOV 2007 - MAR 2008	JCMT 15m	14.5	15.8	Warren et al. 2010

*For our single-dish data, noise was estimated using channels free of emission, while for the literature data cubes, namely for CO(2–1) and CO(3–2), noise was taken from the related papers (see Section 2.2).

in Topal et al. (2016). To define the spatial extent of the emission in CO(2–1) and CO(3–2) transitions, we first defined a region of contiguous source emission in the fully-calibrated and cleaned data cubes (Leroy et al. 2009; Warren et al. 2010). The data cubes were first smoothed spectrally and then smoothed spatially with a full-width at half-maximum (FWHM) equals to that of the beams, i.e. $13''.4$ and $14''.5$ for CO(2–1) and CO(3–2) respectively. We then clipped each (smoothed) cube at 3σ threshold ($3\times$ rms in the smoothed cube) and (smoothed) moment maps were created. The region of contiguous emission for each line was then defined using IDL region-growing algorithm *label_region*. The 3D masks were created from these 2D moment maps. The 3D masks were then applied to the original fully-calibrated CO(2–1) and CO(3–2) data cubes using the Multichannel Image Reconstruction, Image Analysis and Display (MIRIAD) package (Sault et al. 1995) to obtain the moment maps. Please see Section 3.1 in Topal et al. (2016) for more details on defining a region of contiguous emission over a galaxy. The moment maps are shown in Figure 2.

3.2 Beam-averaged quantities

3.2.1 Intensities, line ratios and fluxes

Our CO(1–0) and $^{13}\text{CO}(1-0)$ observations have a beam size of $22''$, while the literature data of CO(2–1) and CO(3–2) have a beam size of $13''.4$ and $14''.5$ respectively. We, therefore, convolved CO(2–1) and CO(3–2) data cubes to a common beam size of $22''$ using MIRIAD task *convol*. We then extracted the spectra from the targeted positions in the cubes using MIRIAD task *imspect*. Gaussian was then fit to the integrated spectra to derive the velocity-integrated CO line intensities in the unit of K km s^{-1} . The single Gaussian function is given by

$$f(v) = A e^{-\frac{(v-v_0)^2}{2\sigma^2}} \quad (1)$$

where $A > 0$ is the flux of the peak at the central (and mean) velocity v_0 , and $\sigma > 0$ is the width of the profile (root mean square velocity). The fits were carried out with the package MPFIT (Markwardt 2009), that employs a Levenberg-Marquardt minimisation algorithm. To avoid local minima, in each case we ran MPFIT several times with different initial guesses. The fitting parameters with the smallest $|1 - \chi_{\text{red}}^2|$ value were taken as the best fit.

CO(1–0) and CO(2–1) were detected (i.e. $S/N > 3\sigma$, where σ is the uncertainty in the integrated line intensities) at all targeted positions. CO(3–2) and $^{13}\text{CO}(1-0)$ were not detected in 5 out of 20 positions, three positions are in common, i.e. positions 12, 13 and 18 where an upper limit for the integrated intensities was estimated

(see Table 3). We estimated the upper limit as $3 \times \sigma \times \Delta V$, where ΔV is the line width of CO(1–0) detected at that position and σ is the rms in the spectra calculated using the channels free of emission. The integrated intensities for all the lines at all positions are listed in Table 3 and the spectra are shown in Figures A1 - A4 in Appendix A.

We estimated the beam-averaged total intensities per unit area I ($\text{W m}^{-2} \text{sr}^{-2}$) and total fluxes F (W m^{-2}) by using the standard expressions below (see also Bayet et al. 2004; Topal et al. 2016):

$$\frac{I}{\text{W m}^{-2} \text{sr}^{-1}} = 1.02 \times 10^{-18} \left(\frac{\nu}{\text{GHz}} \right)^3 \left(\frac{S}{\text{K km s}^{-1}} \right) \quad (2)$$

$$\frac{F}{\text{W m}^{-2}} = \left(\frac{I}{\text{W m}^{-2} \text{sr}^{-1}} \right) \left(\frac{\Omega_{\text{B}}}{\text{sr}} \right) \quad (3)$$

$$\frac{\Omega_{\text{B}}}{\text{sr}} = 1.133 \left(\frac{\theta_{\text{B}}^2}{\text{arcsec}^2} \right) \left(\frac{1}{206265^2} \right) \quad (4)$$

$$\frac{\theta_{\text{B}}}{\text{rad}} = 1.22 \frac{\lambda}{D} \quad (5)$$

where ν and λ are the observed line frequency and wavelength respectively, Ω_{B} is the solid angle sustained by the beam, θ_{B} is the beam size (FWHM) and D is the diameter of the telescope. The beam-averaged total intensities and total fluxes are listed in Table 3.

After obtaining the beam-averaged integrated intensities we calculated the ratios of the integrated line intensities at each position studied throughout the disc of NGC 0628, i.e. $^{12}\text{CO}(1-0) / ^{12}\text{CO}(2-1)$ (hereafter R_{12}), $^{12}\text{CO}(1-0) / ^{12}\text{CO}(3-2)$ (hereafter R_{13}) and $^{12}\text{CO}(1-0) / ^{13}\text{CO}(1-0)$ (hereafter R_{11}). The line ratios are listed in Table 4.

3.2.2 Gas mass and surface density

As shown below, the beam-averaged total molecular gas mass at each position was estimated in the unit of solar mass (M_{\odot}) using the adopted beam, CO-to- H_2 conversion factor (X_{CO}) and the distance to the galaxy,

$$\frac{M_{\text{H}_2}}{M_{\odot}} = 5.5 \times 10^5 \left(\frac{S_{1-0}}{\text{K km s}^{-1}} \right) \quad (6)$$

where S_{1-0} is the integrated intensity of $^{12}\text{CO}(1-0)$ in the unit of K km s^{-1} . We also estimated a surface density, Σ_{H_2} , using S_{1-0} and an adopted X_{CO} value. The X_{CO} value of $2 \times 10^{20} \text{ cm}^{-2} (\text{K km s}^{-1})^{-1}$ ($\alpha_{\text{CO}} = 4.35 M_{\odot} (\text{K km s}^{-1} \text{ pc}^2)^{-1}$, where $\alpha_{\text{CO}} \equiv \Sigma_{\text{H}_2} / S_{1-0}$) was adopted in this study (Dame et al. 2001; Bolatto et al. 2013; Sun et al. 2018). The X_{CO} is related to the

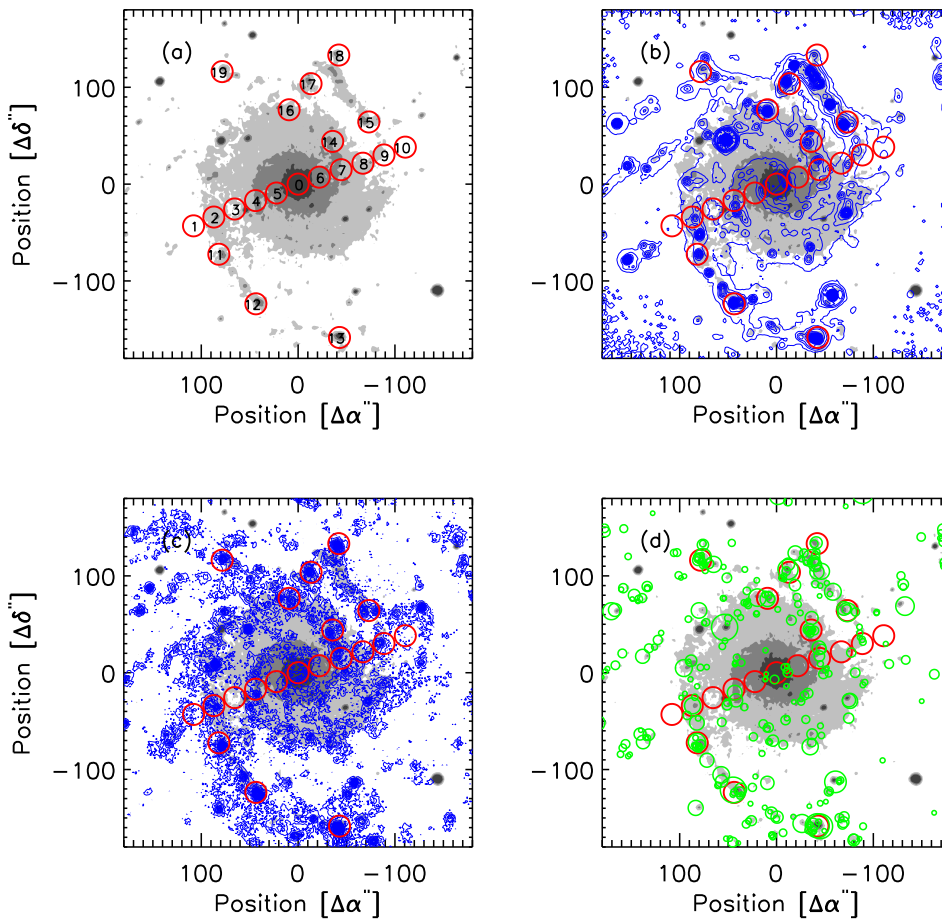


Figure 1. **Panel a:** The targeted positions in the spiral galaxy NGC 0628 are overlaid on an optical image of the galaxy (SDSS). The red circles in each panel indicate the targeted positions with the IRAM 30m beam of $22''$ at 115 GHz. The index numbers for the positions are also shown on the panel as listed in Table 3. **Panel b:** The positions are overlaid on both optical and $24\mu\text{m}$ images of the galaxy (Kennicutt et al. 2003), shown by the greyscale and blue contour respectively. Contour levels on the $24\mu\text{m}$ map are from 1 to 100 per cent of the peak emission in steps of 1 per cent. **Panel c:** The targeted positions and the FUV emission (GALEX; Gil de Paz et al. 2007) are overlaid on the same optical image. Blue contours represent the FUV emission. Contour levels on the FUV map are from 1 to 100 per cent of the peak emission in steps of 2 per cent. **Panel d:** The targeted positions and HII regions (Fathi et al. 2007) are overlaid on the same optical image. The green circles indicate the HII regions. The radius of HII regions ranges from 80 pc to 480 pc at the distance of 7.3 Mpc for the galaxy (Karachentsev et al. 2004). North is up and east to the left in both panels. The offsets are measured with respect to the galaxy centre of $\alpha = 1^{\text{h}}36^{\text{m}}41.7^{\text{s}}$ and $\delta = 15^{\text{d}}47^{\text{m}}1.0^{\text{s}}$ (NED).

beam-averaged H_2 column density (N_{H_2}) as $X_{\text{CO}} = N_{\text{H}_2} / S_{1-0}$. The values of M_{H_2} and N_{H_2} enclosed within the adopted beam and also gas surface density in the unit of $M_{\odot} \text{pc}^{-2}$ at the observed positions are listed in Table 5.

3.3 Modelling and the best model identification

In addition to inferring the physical properties of the molecular gas from the line ratios only, we followed a second approach to quantitatively study the physical properties of the gas, such as density and temperature. We run a radiative transfer code, RADEX (van der Tak et al. 2007). RADEX is a non-LTE radiative transfer code using the large-velocity gradient (LVG) approximation (Sobolev 1960; Castor 1970; Goldreich & Kwan 1974; de Jong et al. 1975). RADEX yields line intensities as a function of a set of user-specified parameters: gas kinetic temperature T_{K} , molecular hydrogen number volume density $n(\text{H}_2)$ and CO number column density per unit line

width $N(\text{CO})/\Delta v$. To create the model grids for ^{12}CO and ^{13}CO lines, we take the Δv as an average FWHM; 18.5 and 17 km s^{-1} for the $\text{CO}(1-0)$ and $^{13}\text{CO}(1-0)$ lines, respectively. Please note that the line widths only minimally affect the model results (van der Tak et al. 2007). We kept the T_{K} , $n(\text{H}_2)$ and $N(\text{CO})$ as free parameters and created the model grids as follows. T_{K} ranges from 5 to 20 K in steps of 1 K to sample the lower temperature regime better, and it ranges from 20 to 250 K in steps of 5 K. $n(\text{H}_2)$ ranges from 10^2 to 10^7 cm^{-3} in steps of 0.25 dex, while $N(\text{CO})$ ranges from 10^{13} to 10^{21} cm^{-2} in steps of 0.25 dex. This produces 42,966 model grids in total for each adopted abundance ratio value (see below).

Stellar evolution and chemical process within the ISM can affect the $[^{12}\text{CO}]/[^{13}\text{CO}]$ abundance ratio. In our analysis, we considered no difference between isotopic ($^{12}\text{C}/^{13}\text{C}$) abundance ratio and isotopologue ($^{12}\text{CO}/^{13}\text{CO}$) abundance ratios. $[^{12}\text{C}]/[^{13}\text{C}]$ abundance ratio ranges widely from the solar neighbourhood to starburst galaxies, from 20 to 90 (Wilson & Rood 1994; Anders & Grevesse 1989; Henkel et al. 1993; Henkel & Mauersberger 1993).

Table 3. Beam-corrected line quantities obtained for each position over the galaxy.

Position	Offset ($\Delta\alpha''$, $\Delta\delta''$)	Radius ^a (arcsec kpc)	Line	$\int T_{\text{mb}} dv$ (K km s ⁻¹)	Total intensity (W m ⁻² sr ⁻²)	Total flux (W m ⁻²)
0	(0, 0)	0 0	¹² CO(1-0)	8.37 ± 0.40	1.31 ± 0.06 × 10 ⁻¹¹	1.69 ± 0.08 × 10 ⁻¹⁹
			¹² CO(2-1)	4.52 ± 0.21	5.65 ± 0.27 × 10 ⁻¹¹	7.28 ± 0.35 × 10 ⁻¹⁹
			¹² CO(3-2)	1.59 ± 0.29	6.72 ± 1.23 × 10 ⁻¹¹	8.66 ± 1.58 × 10 ⁻¹⁹
			¹³ CO(1-0)	1.12 ± 0.14	1.53 ± 0.19 × 10 ⁻¹²	1.97 ± 0.25 × 10 ⁻²⁰
1	(108, 43.1)	116.3 4.1	¹² CO(1-0)	1.70 ± 0.16	2.66 ± 0.24 × 10 ⁻¹²	3.42 ± 0.32 × 10 ⁻²⁰
			¹² CO(2-1)	1.43 ± 0.14	1.79 ± 0.18 × 10 ⁻¹¹	2.31 ± 0.23 × 10 ⁻¹⁹
			¹² CO(3-2)	0.53 ± 0.20	2.25 ± 0.84 × 10 ⁻¹¹	2.90 ± 1.08 × 10 ⁻¹⁹
			¹³ CO(1-0)	0.22 ± 0.08	3.04 ± 1.18 × 10 ⁻¹³	3.92 ± 1.52 × 10 ⁻²¹
2	(87, -34)	93.4 3.3	¹² CO(1-0)	4.74 ± 0.14	7.41 ± 0.22 × 10 ⁻¹²	9.55 ± 0.28 × 10 ⁻²⁰
			¹² CO(2-1)	2.96 ± 0.14	3.69 ± 0.17 × 10 ⁻¹¹	4.76 ± 0.22 × 10 ⁻¹⁹
			¹² CO(3-2)	0.61 ± 0.24	2.59 ± 1.01 × 10 ⁻¹¹	3.34 ± 1.30 × 10 ⁻¹⁹
			¹³ CO(1-0)	0.43 ± 0.06	5.90 ± 0.89 × 10 ⁻¹³	7.61 ± 1.15 × 10 ⁻²¹
3	(65.6, -25.7)	70.4 2.5	¹² CO(1-0)	2.56 ± 0.27	4.00 ± 0.42 × 10 ⁻¹²	5.16 ± 0.54 × 10 ⁻²⁰
			¹² CO(2-1)	2.46 ± 0.15	3.08 ± 0.19 × 10 ⁻¹¹	3.96 ± 0.25 × 10 ⁻¹⁹
			¹² CO(3-2)	0.85 ± 0.24	3.60 ± 0.99 × 10 ⁻¹¹	4.64 ± 1.28 × 10 ⁻¹⁹
			¹³ CO(1-0)	≤ 0.25	≤ 3.41 × 10 ⁻¹³	≤ 4.39 × 10 ⁻²¹
4	(44, -17)	47.1 1.7	¹² CO(1-0)	5.03 ± 0.22	7.86 ± 0.34 × 10 ⁻¹²	1.01 ± 0.04 × 10 ⁻¹⁹
			¹² CO(2-1)	2.98 ± 0.17	3.73 ± 0.22 × 10 ⁻¹¹	4.80 ± 0.27 × 10 ⁻¹⁹
			¹² CO(3-2)	1.31 ± 0.24	5.52 ± 1.01 × 10 ⁻¹¹	7.11 ± 1.30 × 10 ⁻¹⁹
			¹³ CO(1-0)	0.44 ± 0.08	6.02 ± 1.15 × 10 ⁻¹³	7.76 ± 1.49 × 10 ⁻²¹
5	(22.4, -9.2)	24.2 0.9	¹² CO(1-0)	5.22 ± 0.20	8.16 ± 0.31 × 10 ⁻¹²	1.05 ± 0.04 × 10 ⁻¹⁹
			¹² CO(2-1)	3.73 ± 0.17	4.67 ± 0.21 × 10 ⁻¹¹	6.01 ± 0.27 × 10 ⁻¹⁹
			¹² CO(3-2)	1.63 ± 0.36	6.86 ± 1.50 × 10 ⁻¹¹	8.84 ± 1.93 × 10 ⁻¹⁹
			¹³ CO(1-0)	0.52 ± 0.08	7.08 ± 1.11 × 10 ⁻¹³	9.12 ± 1.44 × 10 ⁻²¹
6	(-21.9, 7.2)	23.1 0.8	¹² CO(1-0)	5.28 ± 0.19	8.25 ± 0.30 × 10 ⁻¹²	1.06 ± 0.04 × 10 ⁻¹⁹
			¹² CO(2-1)	3.58 ± 0.18	4.48 ± 0.23 × 10 ⁻¹¹	5.77 ± 0.29 × 10 ⁻¹⁹
			¹² CO(3-2)	0.97 ± 0.19	4.09 ± 0.79 × 10 ⁻¹¹	5.27 ± 1.02 × 10 ⁻¹⁹
			¹³ CO(1-0)	0.50 ± 0.09	6.79 ± 1.21 × 10 ⁻¹³	8.75 ± 1.56 × 10 ⁻²¹
7	(-44.4, 14.9)	46.8 1.7	¹² CO(1-0)	4.94 ± 0.33	7.71 ± 0.51 × 10 ⁻¹²	9.94 ± 0.66 × 10 ⁻²⁰
			¹² CO(2-1)	2.78 ± 0.15	3.47 ± 0.19 × 10 ⁻¹¹	4.47 ± 0.24 × 10 ⁻²⁰
			¹² CO(3-2)	1.03 ± 0.25	4.34 ± 1.04 × 10 ⁻¹¹	5.60 ± 1.34 × 10 ⁻¹⁹
			¹³ CO(1-0)	0.41 ± 0.10	5.64 ± 1.36 × 10 ⁻¹³	7.27 ± 1.75 × 10 ⁻²¹
8	(-66.9, 21.6)	70.3 2.5	¹² CO(1-0)	2.69 ± 0.25	4.20 ± 0.38 × 10 ⁻¹²	5.42 ± 0.50 × 10 ⁻²⁰
			¹² CO(2-1)	2.19 ± 0.15	2.73 ± 0.19 × 10 ⁻¹¹	3.52 ± 0.25 × 10 ⁻¹⁹
			¹² CO(3-2)	1.07 ± 0.37	4.53 ± 1.55 × 10 ⁻¹¹	5.84 ± 1.99 × 10 ⁻¹⁹
			¹³ CO(1-0)	0.28 ± 0.09	3.85 ± 1.20 × 10 ⁻¹³	4.96 ± 1.55 × 10 ⁻²¹
9	(-88.6, 30.1)	93.6 3.3	¹² CO(1-0)	3.82 ± 0.37	5.97 ± 0.58 × 10 ⁻¹³	7.70 ± 0.75 × 10 ⁻²⁰
			¹² CO(2-1)	2.35 ± 0.17	2.93 ± 0.22 × 10 ⁻¹¹	3.78 ± 0.28 × 10 ⁻¹⁹
			¹² CO(3-2)	1.10 ± 0.23	4.62 ± 0.98 × 10 ⁻¹¹	5.96 ± 1.26 × 10 ⁻¹⁹
			¹³ CO(1-0)	0.36 ± 0.13	4.91 ± 1.78 × 10 ⁻¹³	6.32 ± 2.30 × 10 ⁻²¹

^aRadii are calculated with respect to the galaxy centre and given in the units of arcseconds and kpc (i.e. corresponding linear size for the offset with respect to the galaxy centre).

In the Large Magellanic Cloud it is 50 (Wang et al. 2009), while it is $[\text{C}^{12}]/[\text{C}^{13}] > 40$ in starbursts (Martín et al. 2010). Since the abundance ratio shows a radial gradient in galaxies and ranges widely among galaxy types, we consider a range for the abundance ratio instead of taking one single value for all the positions studied. In our model calculations, the abundance ratio ranges from 20 to 90 in steps of 10.

The best model was chosen by applying both χ^2 and likelihood approaches. For the positions where four lines detected, i.e.

3 line ratios are available, reduced χ^2 was defined for each set of model parameters as

$$\chi_r^2 \equiv \sum_i \left(\frac{R_{i,\text{mod}} - R_{i,\text{obs}}}{\Delta R_{i,\text{obs}}} \right)^2, \quad (7)$$

where R_{mod} is the modelled line ratio, R_{obs} is the observed line ratio with uncertainty ΔR_{obs} , and the summation is over all

Table 3. Continued. Beam-corrected line quantities obtained at each position over the galaxy.

Position	Offset ($\Delta\alpha''$, $\Delta\delta''$)	Radius ^a (arcsec kpc)	Line	$\int T_{\text{mb}} dv$ (K km s ⁻¹)	Total intensity (W m ⁻² sr ⁻²)	Total flux (W m ⁻²)
10	(-110.7, 38.2)	117.1 4.1	¹² CO(1-0)	1.74 ± 0.18	2.73 ± 0.28 × 10 ⁻¹²	3.51 ± 0.36 × 10 ⁻²⁰
			¹² CO(2-1)	1.57 ± 0.16	1.97 ± 0.20 × 10 ⁻¹¹	2.54 ± 0.26 × 10 ⁻¹⁹
			¹² CO(3-2)	0.42 ± 0.16	1.79 ± 0.70 × 10 ⁻¹¹	2.31 ± 0.90 × 10 ⁻¹⁹
			¹³ CO(1-0)	≤ 0.20	≤ 2.71 × 10 ⁻¹³	≤ 3.50 × 10 ⁻²¹
11	(81.9, -72.4)	109.3 3.9	¹² CO(1-0)	3.52 ± 0.19	5.49 ± 0.30 × 10 ⁻¹²	7.08 ± 0.39 × 10 ⁻²⁰
			¹² CO(2-1)	2.00 ± 0.15	2.50 ± 0.18 × 10 ⁻¹¹	3.23 ± 0.24 × 10 ⁻¹⁹
			¹² CO(3-2)	≤ 0.63	≤ 2.68 × 10 ⁻¹¹	≤ 3.45 × 10 ⁻¹⁹
			¹³ CO(1-0)	0.25 ± 0.08	3.41 ± 1.14 × 10 ⁻¹³	4.40 ± 1.47 × 10 ⁻²¹
12	(43.6, -123.6)	131.1 4.6	¹² CO(1-0)	2.99 ± 0.22	4.67 ± 0.34 × 10 ⁻¹²	6.02 ± 0.44 × 10 ⁻²⁰
			¹² CO(2-1)	1.67 ± 0.16	2.09 ± 0.20 × 10 ⁻¹¹	2.69 ± 0.26 × 10 ⁻¹⁹
			¹² CO(3-2)	≤ 0.40	≤ 1.70 × 10 ⁻¹¹	≤ 2.20 × 10 ⁻¹⁹
			¹³ CO(1-0)	≤ 0.22	≤ 2.69 × 10 ⁻¹³	≤ 3.82 × 10 ⁻²¹
13	(-42.7, -158.4)	164.1 5.8	¹² CO(1-0)	1.79 ± 0.27	2.80 ± 0.42 × 10 ⁻¹²	3.61 ± 0.54 × 10 ⁻²⁰
			¹² CO(2-1)	1.45 ± 0.16	1.81 ± 0.21 × 10 ⁻¹¹	2.33 ± 0.26 × 10 ⁻¹⁹
			¹² CO(3-2)	≤ 0.53	≤ 2.23 × 10 ⁻¹¹	≤ 2.87 × 10 ⁻¹⁹
			¹³ CO(1-0)	≤ 0.25	≤ 3.43 × 10 ⁻¹³	≤ 4.42 × 10 ⁻²¹
14	(-35.7, 44.1)	56.7 2.0	¹² CO(1-0)	4.38 ± 0.17	6.85 ± 0.27 × 10 ⁻¹²	8.82 ± 0.35 × 10 ⁻²⁰
			¹² CO(2-1)	2.45 ± 0.16	3.06 ± 0.20 × 10 ⁻¹¹	3.94 ± 0.26 × 10 ⁻¹⁹
			¹² CO(3-2)	1.69 ± 0.28	7.13 ± 1.18 × 10 ⁻¹¹	9.18 ± 1.52 × 10 ⁻¹⁹
			¹³ CO(1-0)	0.38 ± 0.08	5.21 ± 1.16 × 10 ⁻¹³	6.72 ± 1.50 × 10 ⁻²¹
15	(-73.1, 64.2)	97.3 3.4	¹² CO(1-0)	5.24 ± 0.18	8.18 ± 0.28 × 10 ⁻¹²	1.05 ± 0.04 × 10 ⁻¹⁹
			¹² CO(2-1)	3.01 ± 0.15	3.76 ± 0.19 × 10 ⁻¹¹	4.84 ± 0.24 × 10 ⁻¹⁹
			¹² CO(3-2)	0.90 ± 0.21	3.79 ± 0.89 × 10 ⁻¹¹	4.88 ± 1.15 × 10 ⁻¹⁹
			¹³ CO(1-0)	0.46 ± 0.09	6.33 ± 1.17 × 10 ⁻¹³	8.16 ± 1.51 × 10 ⁻²¹
16	(9.3, 76.8)	77.3 2.7	¹² CO(1-0)	3.16 ± 0.31	4.94 ± 0.49 × 10 ⁻¹²	6.37 ± 0.63 × 10 ⁻²⁰
			¹² CO(2-1)	2.52 ± 0.14	3.15 ± 0.17 × 10 ⁻¹¹	4.05 ± 0.23 × 10 ⁻¹⁹
			¹² CO(3-2)	1.69 ± 0.28	7.12 ± 1.19 × 10 ⁻¹¹	9.18 ± 1.53 × 10 ⁻¹⁹
			¹³ CO(1-0)	0.68 ± 0.18	9.34 ± 2.42 × 10 ⁻¹³	1.20 ± 0.31 × 10 ⁻²⁰
17	(-13.4, 103.7)	104.6 3.7	¹² CO(1-0)	4.52 ± 0.23	7.06 ± 0.36 × 10 ⁻¹²	9.10 ± 0.46 × 10 ⁻²⁰
			¹² CO(2-1)	2.68 ± 0.15	3.35 ± 0.18 × 10 ⁻¹¹	4.32 ± 0.24 × 10 ⁻¹⁹
			¹² CO(3-2)	0.62 ± 0.18	2.60 ± 0.74 × 10 ⁻¹¹	3.36 ± 0.96 × 10 ⁻¹⁹
			¹³ CO(1-0)	0.34 ± 0.09	4.69 ± 1.27 × 10 ⁻¹³	6.04 ± 1.64 × 10 ⁻²¹
18	(-42, 133.3)	139.7 4.9	¹² CO(1-0)	1.00 ± 0.20	1.56 ± 0.31 × 10 ⁻¹²	2.01 ± 0.40 × 10 ⁻²⁰
			¹² CO(2-1)	0.88 ± 0.11	1.10 ± 0.14 × 10 ⁻¹¹	1.41 ± 0.18 × 10 ⁻¹⁹
			¹² CO(3-2)	≤ 0.49	≤ 2.05 × 10 ⁻¹¹	≤ 2.65 × 10 ⁻¹⁹
			¹³ CO(1-0)	≤ 0.19	≤ 2.66 × 10 ⁻¹³	≤ 3.42 × 10 ⁻²¹
19	(-78.4, 116.2)	140.2 4.9	¹² CO(1-0)	3.73 ± 0.17	5.83 ± 0.27 × 10 ⁻¹²	7.51 ± 0.34 × 10 ⁻²⁰
			¹² CO(2-1)	2.03 ± 0.13	2.54 ± 0.16 × 10 ⁻¹¹	3.27 ± 0.21 × 10 ⁻¹⁹
			¹² CO(3-2)	≤ 0.50	≤ 2.13 × 10 ⁻¹¹	≤ 2.74 × 10 ⁻¹⁹
			¹³ CO(1-0)	0.31 ± 0.07	4.23 ± 1.00 × 10 ⁻¹³	5.46 ± 1.28 × 10 ⁻²¹

^aRadii are calculated with respect to the galaxy centre and given in the units of arcseconds and kpc (i.e. corresponding linear size for the offset with respect to the galaxy centre).

independent line ratios i (one fewer than the number of line ratios available for that position). The model with the smallest χ_r^2 (i.e. $\chi_{r,\text{min}}^2$) was taken as the best model representing the observed line ratios best. For the positions with at least one line has an upper limit integrated intensity, the best model parameters were not obtained, as it would only introduce more uncertainty to actual physical conditions that we are after.

4 RESULTS & DISCUSSION

Although our 22'' beam (778 pc) typically contains many GMCs, we assume that the GMCs within our resolution element have the same average physical properties and the CO transitions are emitted from the same regions. Studying the GMCs using additional emission lines characteristic of star formation, such as UV and infrared (IR) emissions, allows us to probe the physical nature of the gas better. The UV radiation and stellar winds, coming from young

Table 4. Beam-averaged line ratios over the disc of NGC 0628.

Position	Ratio	Value	Position	Ratio	Value
0	R_{12}	1.85 ± 0.13	10	R_{12}	1.11 ± 0.16
	R_{13}	5.25 ± 0.99		R_{13}	4.11 ± 1.65
	R_{11}	7.48 ± 1.02		R_{11}	≥ 8.78
1	R_{12}	1.19 ± 0.16	11	R_{12}	1.76 ± 0.16
	R_{13}	3.19 ± 1.22		R_{13}	≥ 5.54
	R_{11}	7.63 ± 3.04		R_{11}	14.07 ± 4.77
2	R_{12}	1.60 ± 0.09	12	R_{12}	1.79 ± 0.22
	R_{13}	7.72 ± 3.02		R_{13}	≥ 7.40
	R_{11}	10.97 ± 1.69		R_{11}	≥ 13.78
3	R_{12}	1.04 ± 0.13	13	R_{12}	1.24 ± 0.23
	R_{13}	3.00 ± 0.89		R_{13}	≥ 3.39
	R_{11}	≥ 10.26		R_{11}	≥ 7.13
4	R_{12}	1.69 ± 0.12	14	R_{12}	1.79 ± 0.14
	R_{13}	3.85 ± 0.72		R_{13}	2.59 ± 0.44
	R_{11}	11.41 ± 2.24		R_{11}	11.48 ± 2.60
5	R_{12}	1.40 ± 0.08	15	R_{12}	1.74 ± 0.11
	R_{13}	3.21 ± 0.71		R_{13}	5.83 ± 1.39
	R_{11}	10.08 ± 1.63		R_{11}	11.30 ± 2.12
6	R_{12}	1.47 ± 0.09	16	R_{12}	1.26 ± 0.14
	R_{13}	5.45 ± 1.07		R_{13}	1.87 ± 0.36
	R_{11}	10.62 ± 1.94		R_{11}	4.62 ± 1.28
7	R_{12}	1.78 ± 0.15	17	R_{12}	1.69 ± 0.13
	R_{13}	4.79 ± 1.19		R_{13}	7.32 ± 2.12
	R_{11}	11.94 ± 2.98		R_{11}	13.15 ± 3.63
8	R_{12}	1.23 ± 0.14	18	R_{12}	1.14 ± 0.27
	R_{13}	2.50 ± 0.88		R_{13}	≥ 2.05
	R_{11}	9.55 ± 3.11		R_{11}	≥ 5.13
9	R_{12}	1.63 ± 0.20	19	R_{12}	1.84 ± 0.15
	R_{13}	3.49 ± 0.81		R_{13}	≥ 7.40
	R_{11}	10.64 ± 4.00		R_{11}	12.03 ± 2.88

Notes: The exact locations of the positions over the disc of NGC 0628 are shown in Figure 1.

Table 5. Total H₂ mass, column density and gas surface density obtained at each position studied.

Position	M_{H_2} ($M_{\odot} \times 10^5$)	N_{H_2} ($\text{cm}^{-2} \times 10^{20}$)	Σ_{H_2} ($M_{\odot} \text{pc}^{-2}$)	Position	M_{H_2} ($M_{\odot} \times 10^5$)	N_{H_2} ($\text{cm}^{-2} \times 10^{20}$)	Σ_{H_2} ($M_{\odot} \text{pc}^{-2}$)
0	45.9 ± 1.3	16.7 ± 0.8	36.4 ± 1.8	10*	9.6 ± 0.6	3.5 ± 0.4	7.6 ± 0.8
1*	9.3 ± 0.5	3.4 ± 0.3	7.4 ± 0.7	11	19.3 ± 0.6	7.0 ± 0.4	15.3 ± 0.8
2	26.0 ± 0.4	9.5 ± 0.3	20.6 ± 0.6	12	16.4 ± 0.7	6.0 ± 0.4	13.0 ± 0.9
3*	14.1 ± 0.8	5.1 ± 0.5	11.1 ± 1.2	13	9.8 ± 0.8	3.6 ± 0.5	7.8 ± 1.2
4*	27.6 ± 0.7	10.1 ± 0.4	21.9 ± 0.9	14	24.1 ± 0.5	8.8 ± 0.3	19.1 ± 0.8
5*	28.7 ± 0.6	10.4 ± 0.4	22.7 ± 0.9	15	28.7 ± 0.6	10.5 ± 0.4	22.8 ± 0.8
6*	29.0 ± 0.6	10.6 ± 0.4	22.9 ± 0.8	16	17.4 ± 1.0	6.3 ± 0.6	13.8 ± 1.4
7	27.1 ± 1.0	9.9 ± 0.7	21.4 ± 1.4	17	24.8 ± 0.7	9.0 ± 0.5	19.7 ± 1.0
8	14.8 ± 0.8	5.4 ± 0.5	11.7 ± 1.1	18	5.4 ± 0.6	2.0 ± 0.4	4.3 ± 0.9
9*	21.0 ± 1.2	7.6 ± 0.7	16.6 ± 1.6	19	20.5 ± 0.5	7.4 ± 0.3	16.2 ± 0.7

Notes: The positions from 0 to 10 are the positions along the SE-NW cut while the other positions are located in the northern and southern arms of the galaxy (see Fig. 1). The positions indicated with a star symbol are the UV-dim positions, while the rest are the UV-bright positions (see Section 4).

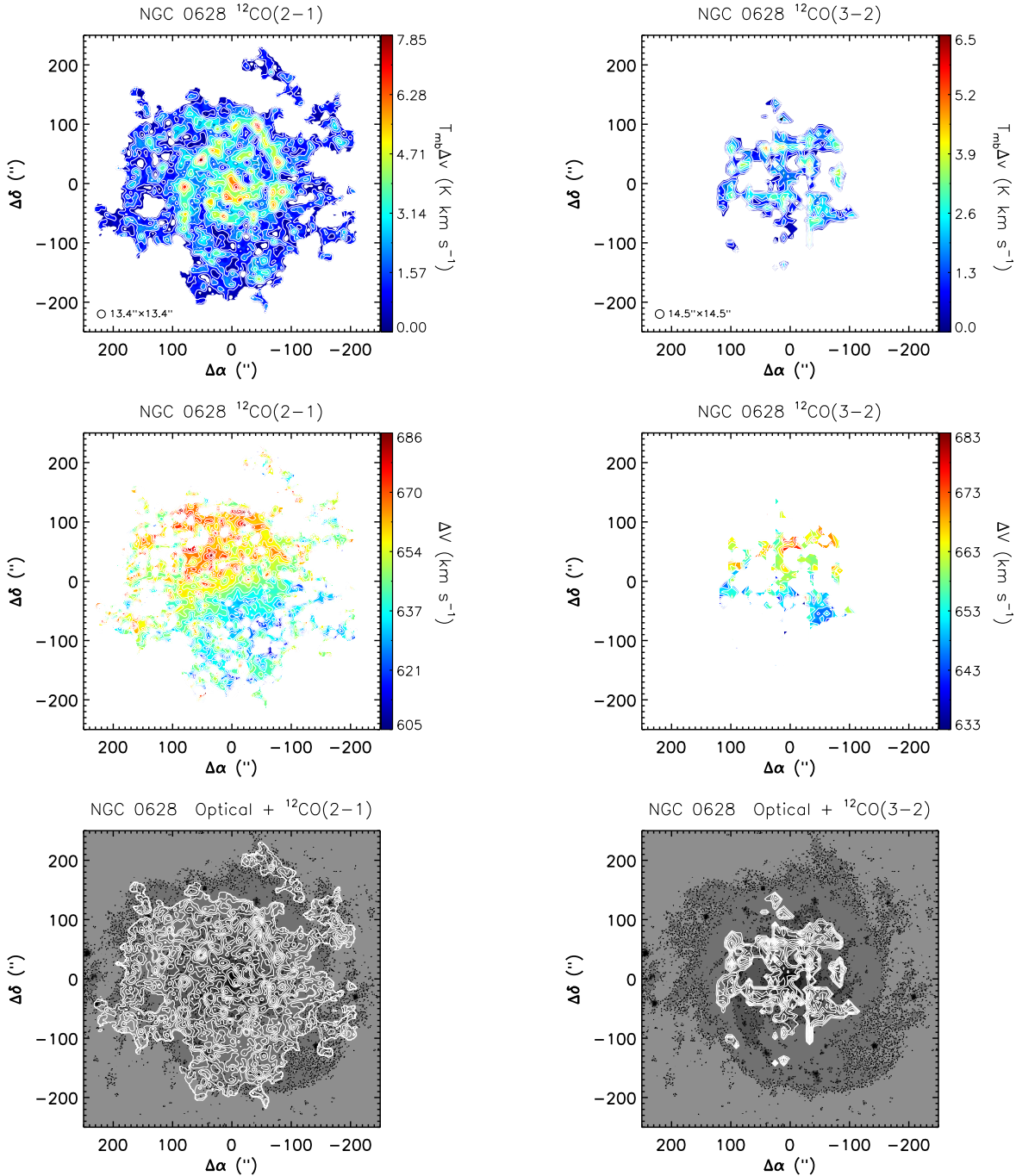


Figure 2. Moment maps from literature data. **Top:** Moment 0 contour maps for CO(2–1) and CO(3–2) respectively. The beam sizes are also shown in the bottom left of each panel. Contour levels on the moment 0 maps are from 10 to 100 per cent of the peak integrated line intensity in steps of 10 per cent. The moment 0 peaks are 7.85 K km s^{-1} and 6.50 K km s^{-1} for CO(2–1) and CO(3–2) respectively. **Middle:** Moment 1 contour maps for CO(2–1) and CO(3–2) respectively. Contour levels on the moment 1 map are spaced by 5 km s^{-1} . **Bottom:** Same moment 0 contour maps (white) of the CO(2–1) and CO(3–2) lines are overlaid on an optical image (greyscale) of the galaxy (SDSS). North is up and east to the left in all images.

O and B stars, can heat the gas and dust, create photon-dominated regions (PDRs) between H II regions and molecular clouds (Hollenbach & Tielens 1999). Also note that FUV radiation from young massive stars can heat the outer layers of a GMC and increase the gas temperature there, up to $\approx 1000 \text{ K}$. However, deeper in the cloud CO could have a lower temperature (e.g. due to dust shielding and H_2 self-shielding), and the hydrogen density should also

relatively be higher (Hollenbach & Tielens 1999). It is, therefore, worth to note that GMC complexes relatively brighter in FUV emission does not necessarily indicate a higher average temperature for the CO gas. Regions with active star formation are usually associated with strong infrared emission coming from the dust heated by massive stars (e.g. Misiriotis et al. 2004; Flores et al. 2004), and it is known that the $24\mu\text{m}$ emission is sensitive to the star forma-

tion rate (e.g. Gordon et al. 2004; Calzetti et al. 2005). However, shock waves from supernova explosions and strong stellar winds could make the regions of active star formation inhospitable for dust, causing only the foreground dust to survive (Calzetti et al. 1996).

The positions from 11 to 19, i.e. the locations in the northern and southern arms of the galaxy (see Fig. 1), were chosen based on being relatively brighter in the GALEX UV image (hereafter initially selected UV-bright positions) compared to the positions over the cut (i.e. the positions from 0 to 10). We calculated the Gaussian weighted total FUV, 24 μ m, 70 μ m, and 160 μ m fluxes at each position as follows. After applying unit conversions necessary to Spitzer and GALEX data, we obtained all the data in the unit of Jy. We then multiplied the flux in each pixel by a 2D Gaussian weighting function of FWHM equal to that of the adopted beam (and centred at each position). Finally, the total 24 μ m, 70 μ m, 160 μ m, and FUV fluxes for each position were calculated by summing Gaussian weighted fluxes in all pixels in each image.

Based on the estimated total FUV fluxes, we defined the positions either UV-bright or UV-dim as follows. Any positions over the radial cut (i.e. the positions from 0 to 10) with an FUV flux lower than the lowest FUV flux found among the initially selected UV-bright positions (i.e. the positions from 11 to 19) are defined as the UV-dim positions. As a result, all positions outside the radial cut and the positions 0, 2, 7, and 8 are considered as UV-bright positions while the rest, namely the positions 1, 3, 4, 5, 6, 9, and 10 are considered as UV-dim positions. The discussions will be made based on this grouping in the upcoming sections.

As seen from Figure 1, the UV-bright positions include more H II complexes compared to the UV-dim positions, and most positions brighter in the 24 μ m image are also brighter in the UV. These observational characteristics, therefore, indicate that the star formation activity could be stronger at the UV-bright positions than that of the UV-dim positions. This allows us to probe the effects of UV radiation on molecular clouds. However, the effects of extinction to the observable UV should first be considered to understand better the reason(s) behind the difference in the UV-brightness seen among the positions studied (see Figure 5). Additionally, probing the line ratios at the positions chosen side by side over the SE-NW cut enables us to study any radial variations in physical conditions of the gas from the centre to the outskirts of the galaxy without selection bias.

4.1 Intensities and molecular line ratios

4.1.1 Intensities

The change in the velocity-integrated CO line intensities and related line ratios across the positions studied are shown in Figure 3. As seen from panel *a* of Figure 3, the central region is the brightest in CO emission. The CO integrated line intensities show a decrease, with some fluctuations, as a function of radius from the centre of the galaxy up to 165'' or a linear distance of about 5.8 kpc (see panel *a* in Figure 3 and Table 3). When we consider the positions over the SE-NW cut only, the decrease is more clearly seen on both sides of the cut (see panel *b* in Figure 3). The CO(1-0) integrated intensities at some UV-bright positions show an increase in respect to the general trend, causing more fluctuations in the ratios after about 70'' from the centre (see panel *a* of Fig. 3).

4.1.2 $^{12}\text{CO}/^{13}\text{CO}$ ratio

The CO(1-0) has an upper-level energy temperature of ≈ 5.5 K, while it is ≈ 16.5 K and ≈ 33 K for CO(2-1) and CO(3-2) respectively. Since CO(3-2) requires a denser environment compared to CO(1-0) and CO(2-1), it traces not only warmer but also slightly more compact regions of the gas cloud. As seen from panel *c* of Figure 3 and Table 4, the R_{13} ratios across the entire disc are always higher than the R_{12} ratios indicating that CO(2-1) transition is brighter than CO(3-2) at all positions studied. Additionally, the R_{13} ratios show larger fluctuations than that of the R_{12} ratios.

The R_{12} ratios range from 1 to 2 at all positions studied except the positions 3, 10, and 18, where the ratio could slightly get less than 1. The average R_{12} ratio over the disc of NGC 0628 is 1.51 ± 0.02 (excluding the lower limits). If we consider the UV-bright positions only, the average R_{12} ratio is 1.59 ± 0.02 , while it is 1.36 ± 0.04 at the UV-dim positions (excluding the lower limits). These results indicate that the UV-dim positions have a lower R_{12} ratio (relatively warmer gas) compared to that of the UV-bright positions (relatively colder gas).

While we detected CO(1-0) at all 20 positions studied, the CO(3-2) was detected at 15 positions over the galaxy, i.e. all UV-dim positions and 8 UV-bright positions (see Table 3 and panel *a* in Figure 1). As a result, the R_{13} ratio was obtained at 75% of the positions studied, while the R_{13} ratios in the remaining 5 positions are just a lower limit. The range for the R_{13} ratios is wider ($2 \leq R_{13} \leq 10.7$) than that for the R_{12} ratios ($1 \leq R_{12} \leq 2$). The R_{13} ratios at all positions studied are higher than 2, except positions 1, 8 and 16 where the ratios could get lower, given the error bars (see Table 4). The average R_{13} ratio over the disc of NGC 0628 is 4.3 ± 0.1 (excluding the lower limits). The average ratio at the UV-bright positions is $R_{13} = 4.74 \pm 0.28$ while it is 3.76 ± 0.12 at the UV-dim positions. The lower average ratio at the UV-dim positions indicates the existence of relatively warmer gas compared to that of the UV-bright positions.

The R_{12} line ratio in the Milky Way and nearby galaxies typically spans between 1 – 1.5 (e.g. Hasegawa 1997; Leroy et al. 2009), similar to the range we found in the disc of NGC 0628. Mao et al. (2010) obtained R_{13} ratios in the central region of 61 galaxies (i.e., spirals, starbursts, Seyferts, and luminous infrared galaxies) and found no correlation for R_{13} ratio to Hubble types. The range of R_{13} ratios that we found in the disc of NGC 0628 is wider than that of 61 galaxies ($0.5 \leq R_{13} \leq 5$; Mao et al. 2010). In their sample, there are ten normal spirals with $R_{13} > 1$, while starbursts can have a ratio as low as 0.5 (Mao et al. 2010). The R_{13} ratios across the disc of NGC 0628 are, therefore, similar and even higher compared to those found in the centre of normal spirals. Since the lower the R_{13} ratios, the more enhanced the molecular excitations, the positions we studied in the disc of NGC 0628, have similar or even colder ISM concerning the centre of normal spirals, and particularly that of starbursts.

As discussed above, the UV-bright positions (hosting more H II regions) in NGC 0628 have higher R_{12} and R_{13} ratios (lower temperature) compared with the UV-dim positions over the cut, where the feedback from massive stars seems to affect the physics of the GMCs relatively weakly (see panel *c* of Figure 1). This indicates the existence of colder gas in GMCs surrounded by more H II regions at the UV-bright positions. However, at the UV-dim positions, there is slightly warmer gas bathed in GMCs with less number of H II regions.

4.1.3 $^{12}\text{CO}/^{13}\text{CO}$ ratio

In molecular clouds, ^{13}CO is generally less abundant and optically thin compared to its parent molecule ^{12}CO . The R_{11} ratios, therefore, trace diffuse gas, i.e. the larger the R_{11} ratio, the thinner the CO gas (and vice-versa). Feedbacks from star formation activities, such as supernova explosions, strong UV radiation from massive stars and H II regions could make the gas more diffused. As a first thought, we might, therefore, expect to find higher R_{11} ratios, so more diffused gas at the UV-bright positions where star formation activity seems to be stronger compared to the UV-dim positions.

As seen from Figure 3, the R_{11} ratios show more fluctuations as a function of radius compared to that of R_{12} and R_{13} ratios. As listed in Table 4, the average R_{11} ratio over the disc of NGC 0628 is 10.5 ± 0.2 (excluding the lower limits). The average R_{11} ratio is 10.66 ± 0.28 at the UV-bright positions, while it is 10.08 ± 0.29 at UV-dim positions (excluding the lower limits), indicating a slightly higher ratio, so more diffused gas, at the UV-bright positions. Please note that the UV-bright positions include significantly more H II regions and brighter at $24\mu\text{m}$ emission compared to the UV-dim positions (see Figure 1). It is, therefore, natural to suggest the existence of a high level of star formation activity and in turn, dominant effects of massive stars in the ISM of the UV-bright positions. Thereupon the intense star formation activity could cause the high R_{11} ratio, so the more diffused gas, seen at the UV-bright positions.

The R_{11} ratio increases up to about $50''$ (or equally ≈ 1.7 kpc) and then starts to fluctuate (see panel *c* Fig. 3). However, the R_{13} ratio steadily decreases up to about $50''$ as opposed to the R_{11} ratio; it then starts to fluctuate. A closer look at the ratios on both sides of the SE-NW cut reveals the same trend; while the R_{11} ratio increases up to about $50''$, the R_{13} ratio decreases (please see panel *d* in Figure 3). This indicates that the gas is getting thinner and warmer from the centre through the outskirt up to 1.7 kpc. However, the decrease in R_{13} ratios through the NW part of the cut is happening more slowly compared to the SE part of the disc (see panel *d* of Figure 3).

The range of R_{11} ratios in NGC 0628 is $5 \leq R_{11} \leq 19$, given the error bars (see Table 4). This range is similar to the range found for the centre of spirals ($5 \leq R_{11} \leq 20$, Paglione et al. 2001) and Seyferts ($8 \leq R_{11} \leq 17$, Henkel et al. 1994; Meier et al. 2008; Israel 2009a,b). However, the range of R_{11} ratios in NGC 0628 is narrower than what is found for the centre of lenticular galaxies ($3 \leq R_{11} \leq 30$; Krips et al. 2010, Crocker et al. 2012 and Topal et al. 2016) and starbursts ($10 \leq R_{11} \leq 33$; Aalto et al. 1995 and Baan et al. 2008). This supports the idea that when the star formation is high, the gas gets thinner, so the R_{11} ratio gets higher, as we usually see in starbursts and some lenticulars with an unexpectedly high amount of molecular gas. However, although we found a narrower range for R_{11} ratios compared to that of starbursts and some lenticulars, there are essentially some starbursts and lenticulars with similar line ratios at their centres compared to what we found in the disc of NGC 0628. These results lead us to the following conclusion. The level of star formation activity and feedbacks should be the main driver defining the line ratios, regardless of galaxy types, i.e. positions in the arms or inter-arms of any types of galaxies may reveal similar molecular line ratios to that found at different positions over different types of galaxies. However, the central region of different types of galaxies could have different line ratios as the physics of the ISM could be driven by a different phenomenon in their centres, e.g. the existence of an active galactic nucleus (AGN). The R_{11} ratio at the centre of NGC 0628 is

7.48 ± 1.02 (see Table 4), which is indeed different and lower than the ratios seen in starbursts (e.g. Aalto et al. 1995; Baan et al. 2008).

4.2 Total H_2 mass and extinction

Because of its low critical density ($n_{\text{crit}} \approx 10^3 \text{ cm}^{-3}$), CO is generally thought to be a good tracer for the total gas mass in galaxies. As seen in Table 5, the central region of NGC 0628 has the highest amount of molecular gas confined within the adopted beam of $22''$. The average total gas mass and gas surface density at the UV-bright positions are $M_{\text{H}_2} = 21.6 \pm 0.8 \times 10^5 M_{\odot}$ (with a median value of $M_{\text{H}_2} = 20.5 \pm 0.5 \times 10^5 M_{\odot}$) and $\Sigma_{\text{H}_2} = 17.1 \pm 0.6 M_{\odot} \text{ pc}^{-2}$ (with a median value of $\Sigma_{\text{H}_2} = 16.2 \pm 0.7 M_{\odot} \text{ pc}^{-2}$), respectively. On the other hand, average molecular gas mass and gas surface density at the UV-dim positions are $M_{\text{H}_2} = 19.9 \pm 1.3 \times 10^5 M_{\odot}$ (with a median value of $M_{\text{H}_2} = 21.0 \pm 1.2 \times 10^5 M_{\odot}$) and $\Sigma_{\text{H}_2} = 15.8 \pm 1.0 M_{\odot} \text{ pc}^{-2}$ (with a median value of $\Sigma_{\text{H}_2} = 16.6 \pm 1.6 M_{\odot} \text{ pc}^{-2}$), respectively. These results indicate that the UV-bright and UV-dim positions have similar molecular gas mass and gas surface density. This is true even after excluding the positions 0 and 18, where the beam-averaged total molecular gas mass has the highest and the lowest values, respectively. Panel *a* of Figure 4 indicates that M_{H_2} decreases as a function of galactocentric radius following the same pattern as seen in the integrated intensities (see panel *b* of Figure 3). The same trend is seen for Σ_{H_2} and N_{H_2} as a function of radius (see Table 5). The panels *b*, *c*, and *d* of Figure 4 indicate that there is a linear correlation between the beam-averaged total molecular gas mass and extinction (i.e. the IR-to-FUV ratio): as the IR-to-FUV ratio increases the molecular gas mass also increases. It is also worth to note that the metallicity can strongly affect the CO-to- H_2 conversion factor used to estimate the total beam-averaged H_2 mass (Glover & Clark 2012). Effects of both shielding and metallicity, which are not within the scope of this study, play an essential role in determining the molecular gas content of GMCs.

As seen from panel *a* of Figure 5, the IR-to-FUV ratio decreases as a function of the galactocentric radius, similar to the molecular gas mass. As revealed by panel *b* of Figure 5, there is a linear correlation between UV-brightness and $24\mu\text{m}$ emission, and most positions brighter at $24\mu\text{m}$ emission are the UV-bright positions. However, both groups of positions share a similar range for $160\mu\text{m}$ fluxes (see the embedded figure in panel *b* of Figure 5). The panels *c* and *d* of Figure 5 show that as the UV-brightness decreases, the IR-to-FUV ratio increases, considering the all positions studied. Since UV-bright positions are brighter at both UV and $24\mu\text{m}$ emission, and UV-dim positions are the opposite, both groups of positions share a similar range for $F_{24\mu\text{m}}/F_{\text{FUV}}$ ratios (see panel *c* of Fig. 5). However, the $F_{160\mu\text{m}}/F_{\text{FUV}}$ ratio is higher at almost all UV-dim positions (panel *d* of Figure 5). The reason for this difference in the ratio is that the UV-bright positions have stronger FUV radiation field, so more young massive OB stars in their ISM (also indicated by stronger $24\mu\text{m}$ emission and hosting more H II regions), compared to the UV-dim positions. A high value of $F_{160\mu\text{m}}/F_{\text{FUV}}$ could indicate two possible scenarios. Firstly, the extinction at the UV-dim positions could be dominant and absorb the FUV, and thus depressing the F_{FUV} . Secondly, star formation efficiency at the UV-dim positions could be lower, causing weaker UV radiation field. The second scenario is a more plausible explanation for the UV-dim positions. $24\mu\text{m}$ emission is a good tracer for warm gas with temperature approaching 100 K (possibly heated by star formation). The weakness in $24\mu\text{m}$ emission, there-

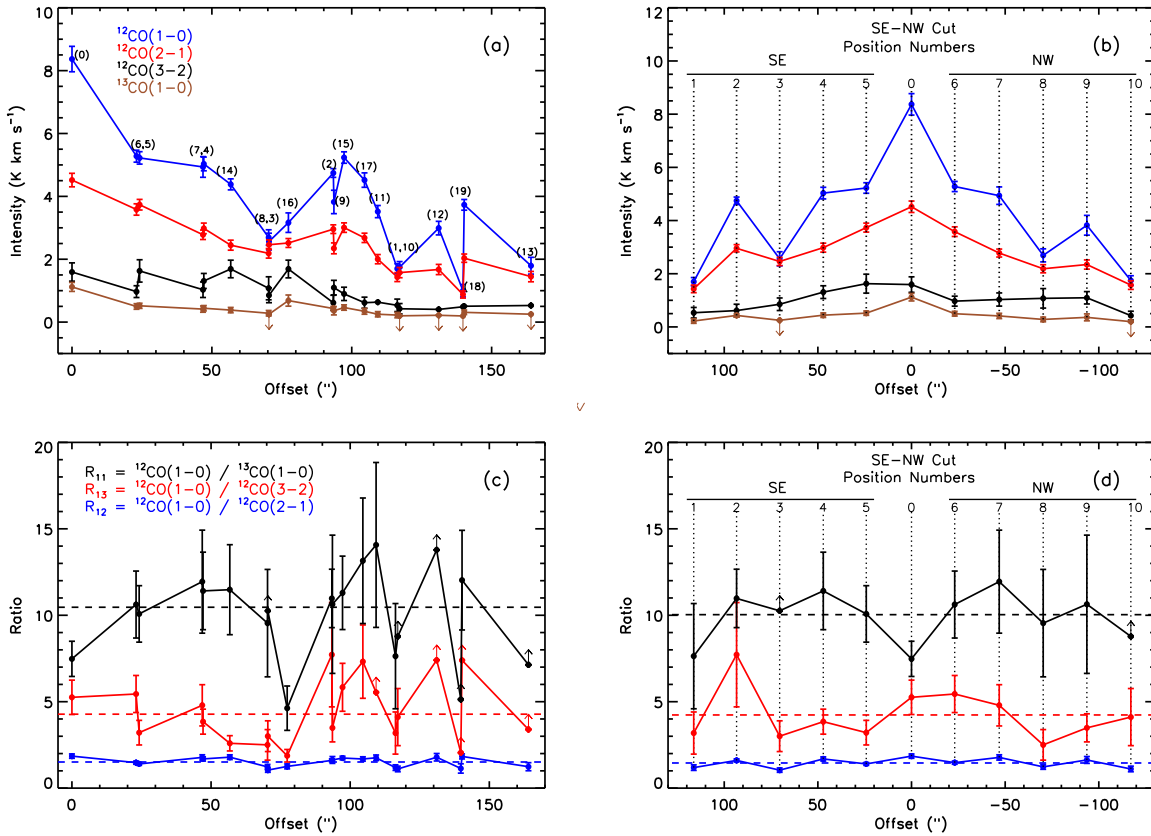


Figure 3. **Panel a:** The integrated intensities at all positions are shown as a function of distance from the galaxy centre. The position numbers (also listed in Table 3) are also indicated in parentheses. **Panel b:** The same as panel a but for the positions along the SE-NW cut only. The integrated intensities across the SE-NW cut are shown (please see panel a in Figure 1 and Table 3). **Panel c:** The line ratios obtained at all positions along the disc of NGC 0628 are shown as a function of distance from the galaxy centre. From the centre to the most distant position observed, the same position numbers applied, as shown in the top left panel. The average value for each group of line ratios (excluding the lower limits, see Table 4), namely R_{12} , R_{13} and R_{11} , is also shown with dashed lines. **Panel d:** The same as the panel c but for the positions along the SE-NW cut only. The position numbers are also indicated for both SE and NW parts of the cut.

fore, indicates that there is not much FUV (so not much star formation) to make the dust warm enough at the UV-dim positions. This could cause the $F_{160\mu\text{m}}/F_{\text{FUV}}$ ratio to be higher at those positions compared to the UV-bright ones (see panel d of Fig. 5). On the contrary, the UV-bright positions (which are brighter at $24\mu\text{m}$ emission and include much more H II regions) have lower $F_{160\mu\text{m}}/F_{\text{FUV}}$ ratios, as expected given the higher FUV fluxes they have. All this evidence lead us to the following conclusion. The reason for the difference in the UV-brightness seen between these two groups of positions, namely UV-bright and UV-dim positions, is not likely the extinction, but having a different level of star formation activity. The IR-to-UV ratio is also sensitive to metallicity, luminosity, and some other factors (Dale et al. 2007), but these factors are not within the scope of the present study.

4.3 Modelling

The present model results are the best we can do with the current data. Nevertheless, we discuss the usage of a single-component model for the ISM where many phenomena are at play, such as magnetic fields, gas self-gravity, turbulent velocity field, UV radiation field, cosmic rays, dust shielding and gas self-shielding. First and foremost, not only higher transitions of CO, i.e. CO(4–3) and

higher, but also multiple lines of high-density tracers, such as HCN, HCO^+ , HNC, and HNCO are required to probe denser and warmer components of the gas complexes better (e.g. Topal et al. 2016). Secondly, having multiple lines of such molecules is particularly important as some studies show that divergence could be present in the spectral line energy distributions (SLEDs) after $J = 4 - 3$, while it usually shows a similar trend up to $J = 3 - 2$, indicating different gas conditions and dense gas fractions (e.g. Papadopoulos et al. 2014). Finding the most likely SLED representing the observed line ratios best, therefore, highly depends on the availability of high- J transitions. Consequently, given the complex nature of the gas clouds, applying a single-component model with low- J transitions of CO molecule using RADEX (or similar radiative transfer codes) can only give us some insights on the average physical conditions of relatively colder and less dense gas in the ISM. Although these caveats are important to point out, the present study provides valuable information on the physical nature of the relatively colder and less dense gas over the disc of NGC 0628 for future references. Keeping these caveats in mind, we now discuss the model results in the following.

13 out of 20 positions were investigated by applying the LVG modelling. 8 out of 13 positions are UV-bright positions (i.e. the positions 0, 2, 7, 8, 14, 15, 16 and 17), while the rest are UV-dim

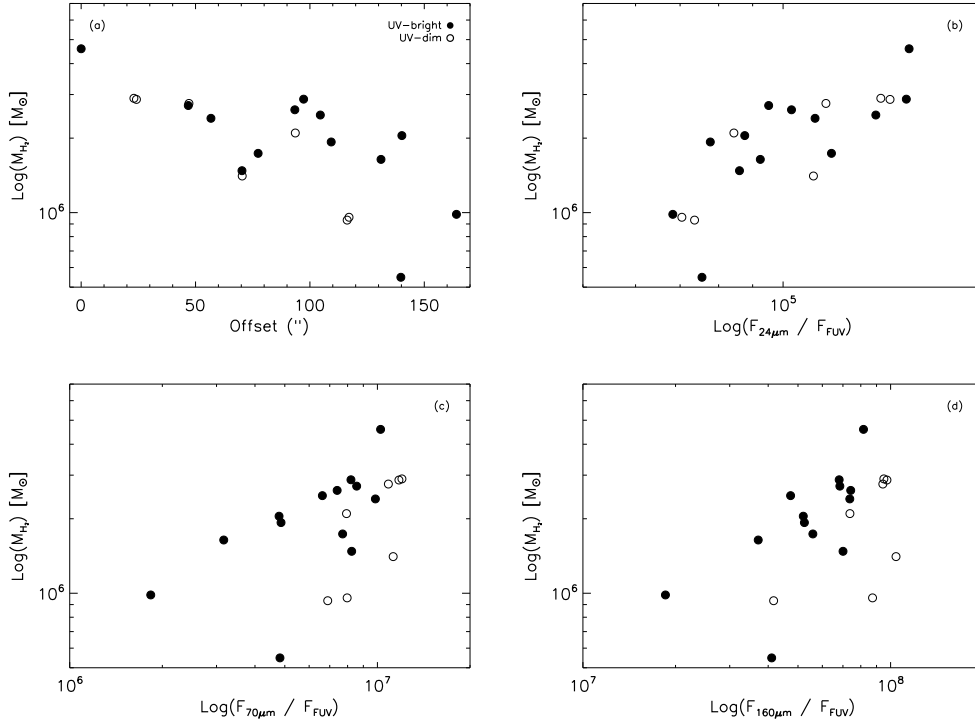


Figure 4. **Panel a:** The beam-averaged total molecular gas mass as a function of distance from the galactic centre is shown. **Panels b, c and d:** The IR-to-FUV ratio as a function of molecular gas mass is shown. The open circles represent the UV-dim positions while the filled circles represent the UV-bright positions (see the text).

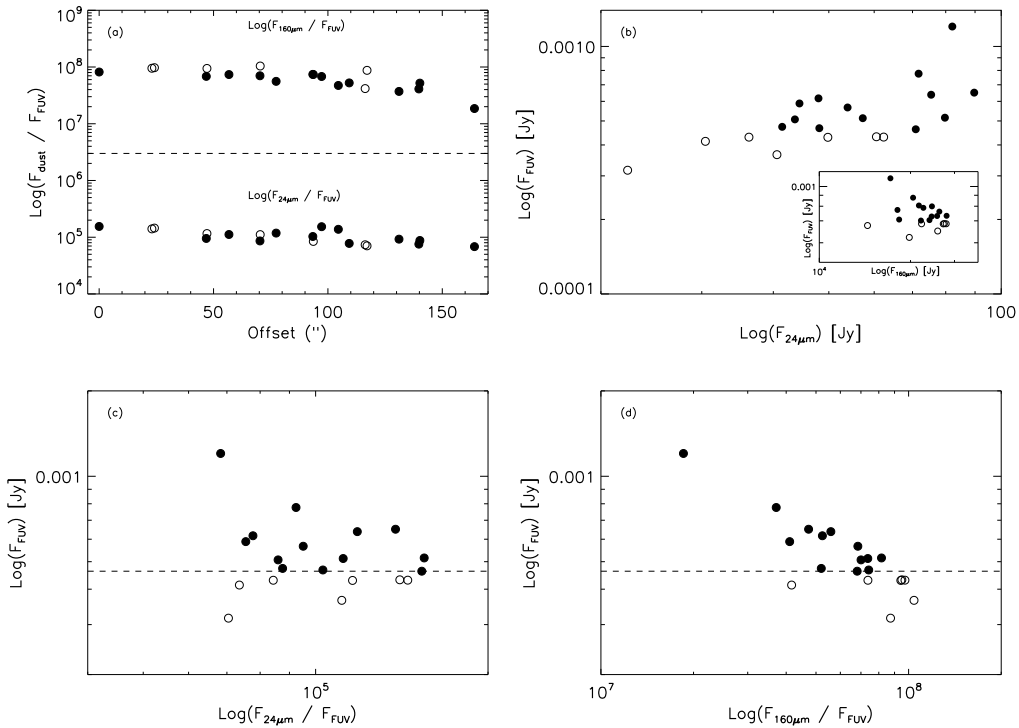


Figure 5. **Panel a:** The extinction as a function of distance from the galactic centre. **Panel b:** The beam-averaged 24 μ m and 160 μ m (the embedded figure) fluxes are shown as a function of FUV flux. **Panels c and d:** The extinction for 24 μ m and 160 μ m emission is shown as a function of FUV flux. The dashed line shows the position with the lowest FUV flux among the initially selected UV-bright positions located outside the cut (see the text). The filled symbols represent the UV-bright positions while the open symbols stand for the UV-dim positions in all panels.

positions located over the cut (i.e. the positions 1, 4, 5, 6, and 9). Our LVG model results, based on both χ^2 and likelihood methods, are listed in Table 6, $\Delta\chi^2$ contour maps are shown in Figure A5, and the probability distribution functions (PDFs) for each model parameter are shown in Figure A6.

As seen from Figure A5, the $\Delta\chi_{r,\min}^2$ contour maps reveal the classical banana-shaped degeneracy, i.e. inverse $n(\text{H}_2)$ - T_K relationship (e.g. van der Tak et al. 2007; Topal et al. 2014; Papadopoulos et al. 2014; Topal et al. 2016). The most PDFs reveal either a half or a full single-peaked Gaussian profile, resulting in a good agreement between the peak and the median of the likelihood (see Figure A6). T_K and $n(\text{H}_2)$ mostly show a half-Gaussian PDF, i.e. a peak at low values followed by a gradual decrease in the PDF as the values increase, while $N(\text{CO})$ mostly shows a complete Gaussian PDF (see Figure A6). As a result, the best-fitting model (in a χ^2 sense) is mostly contained within the 68 per cent (1σ) confidence levels for all three parameters regardless of the shape of the PDFs, except a few positions (see Table 6 and Figure A6).

The range for the T_K is large at some positions across the disc of NGC 0628. This is partially due to the classical banana-shaped degeneracy seen in the χ^2 contour maps and flatness seen in the PDFs (see Figure A5 and Figure A6), causing large uncertainties in the model results at some positions (see Table 6). However, the limit values can still provide us with valuable information on possible differences in temperature from one position to another. The results from both χ^2 and likelihood methods indicate that T_K at position 14 is not higher than 30 K, and it could get even lower at position 17. The temperature at these UV-bright positions could be as low as 5 – 6 K, making them the coldest among the positions studied. However, the temperature at UV-dim positions 4, 5, and 9, and UV-bright position 7 is always higher than 30 K, making them the hottest compared to the other positions studied. The UV-bright positions 0 (the centre) and 15 reveal a similar range for the T_K ; ranging from 20 to 100 K, while the range for UV-dim positions 1 and 9 could be wider; 20 to 200 K. The temperature at the remaining UV-bright positions 2, 8 and 16, and the UV-dim position 6, where the results from both methods do not overlap, indicates an even wider range from about 10 to 200 K, making these positions more uncertain in terms of temperature. Even though the model results suggest larger uncertainties in the temperature at some positions, the empirical (see Section 4.1.2) and model results are mostly in agreement; the UV-bright positions mostly have lower temperature compared to that of the UV-dim positions. However, more positions in the disc of the galaxy should be studied to make a firmer conclusion.

$n(\text{H}_2)$ and $N(\text{CO})$ also show large variations throughout the disc of the galaxy. The best model and most likely model results do not overlap at positions 1, 4, 7 and 9 for $n(\text{H}_2)$, and positions 2, 8 and 16 for $N(\text{CO})$. Except for these positions, the best model results (in a χ^2 sense) are within 1σ uncertainty of the median of the likelihood for both parameters, i.e. $n(\text{H}_2)$ and $N(\text{CO})$ at the remaining positions (see Table 6). As seen from Table 6, the UV-bright positions 0 and 15, and the UV-dim positions 4, 5 and 6 have similar $n(\text{H}_2)$ and $N(\text{CO})$ values. However, considering the results from both methods, namely χ^2 and likelihood, most UV-bright positions (i.e. the positions 8, 14, 16, and 17) have higher $n(\text{H}_2)$ and $N(\text{CO})$ compared to the UV-dim positions.

Overall, based on both χ^2 and most likely model results, while the UV-dim positions mostly have warmer ISM with relatively lower $N(\text{CO})$ and $n(\text{H}_2)$, the UV-bright positions indicate an opposite trend, i.e. colder ISM with higher $N(\text{CO})$ and $n(\text{H}_2)$. These model results agree with the results based on empirical line ratios.

5 CONCLUSIONS

We studied 20 positions across the disc of a spiral galaxy NGC 0628. 11 out of 20 positions were selected over the SE-NW cut, while the rest of the positions were selected in the southern and northern arms of the galaxy. 13 out of 20 positions are brighter in the UV and hosting more H II regions compared to the UV-dim positions with opposite characteristics. This enables us to probe; i) radial variations in the physical conditions of the gas; ii) differences in the physical conditions between the UV-bright and UV-dim positions; iii) correlations between strong star formation activity indicators (such as UV, IR radiation and H II regions) and molecular gas if any. Our main conclusions are summarised below.

(i) Our beam-averaged velocity-integrated CO line intensities indicate that the central region of NGC 0628 is brighter in CO compared to the positions in the arms and inter-arms of the galaxy. The CO intensity decreases steadily with some fluctuations as a function of radius up to 5.8 kpc from the centre. The decrease is more clearly seen on both sides of the SE-NW cut.

(ii) The range for the R_{13} ratios is wider than that for R_{12} ratios in NGC 0628, and the R_{12} ratios show a smoother distribution with smaller uncertainties across the disc of the galaxy. The R_{12} ratios range from 1 to 2, with an average value of 1.51 ± 0.02 , while the R_{13} ratios range from 2 to 10, with an average value of 4.3 ± 0.1 across the disc of NGC 0628. The UV-dim positions have lower R_{12} and R_{13} ratios (relatively warmer gas) whereas the UV-bright positions have higher ratios (relatively colder gas).

(iii) The R_{11} ratios, as a tracer for diffused gas, show more fluctuations compared to that of R_{12} and R_{13} ratios in NGC 0628. The R_{11} ratio increases up to $50''$ (or equally 1.7 kpc) and then starts to fluctuate with a tendency to decrease. In contrast with the increase in the R_{11} ratios, the R_{13} ratios decrease, indicating that the gas gets warmer and thinner up to 1.7 kpc. Outside the central 1.7 kpc, CO(1–0) integrated intensity at some UV-bright positions shows an increase causing sudden decrease and increase in the ratios.

(iv) The range of R_{12} and R_{13} ratios along the disc of NGC 0628 is similar to that found in the centre of spirals, like our own Milky Way, indicating similar gas temperatures. The range of R_{13} ratios is wider than that found in the centre of 61 galaxies from different Hubble types. The R_{13} ratios in the disc of NGC 0628 are higher than that found at the centre of starbursts, indicating that NGC 0628 has relatively colder ISM. The range of R_{11} ratios in NGC 0628 is $5 \leq R_{11} \leq 19$ given the error bars, similar to that found in the central regions of spirals and Seyferts. While the R_{11} ratios at some positions in the arms and inter-arms of NGC 0628 are similar to that found at the centre of starbursts, it is lower in the centre of the galaxy.

(v) Beam-averaged molecular gas mass and the gas surface density at the centre of the galaxy is the highest. As expected from the decrease seen in the integrated line intensities, there is also a decrease in M_{H_2} , Σ_{H_2} and N_{H_2} as a function of the radius from the centre of the galaxy. We found that the UV-bright and UV-dim positions have similar beam-averaged total molecular gas mass and gas surface densities on average. We also found that there is a linear correlation between the molecular gas mass and the extinction (i.e. IR-to-FUV ratio).

(vi) The extinction decreases as a function of galactocentric radius similar to the molecular gas mass. UV-bright and UV-dim positions have similar $F_{24\mu\text{m}}/F_{\text{FUV}}$ ratios, while the $F_{160\mu\text{m}}/F_{\text{FUV}}$ is higher at the UV-dim positions. This is due to the fact that UV-bright positions are brighter at both $24\mu\text{m}$ and UV, while UV-dim positions are dimmer at both wavelengths, but they have similar

Table 6. Model results for the CO gas in the disc of NGC 0628.

Position	Offset ($\Delta\alpha''$, $\Delta\delta''$)	Parameter	χ^2	Likelihood	Position	Offset ($\Delta\alpha''$, $\Delta\delta''$)	Parameter	χ^2	Likelihood
0	(0, 0)	T_K	30 K	$38.4^{+38.7}_{-18.6}$ K	8	(-66.9, 21.6)	T_K	8 K	$100.7^{+96.6}_{-73.9}$ K
		$\log(n(\text{H}_2))$	2.2 cm^{-3}	$2.5^{+0.7}_{-0.4} \text{ cm}^{-3}$			$\log(n(\text{H}_2))$	5.2	$3.6^{+2.4}_{-1.2} \text{ cm}^{-3}$
		$\log(N(\text{CO}))$	17.7 cm^{-2}	$17.7^{+0.2}_{-0.3} \text{ cm}^{-2}$			$\log(N(\text{CO}))$	17.2 cm^{-2}	$18.4^{+1.6}_{-0.9} \text{ cm}^{-2}$
		$[^{12}\text{C}]/[^{13}\text{C}]$	20				$[^{12}\text{C}]/[^{13}\text{C}]$	20	
1	(108, -43.1)	T_K	25 K	$86.9^{+98.9}_{-62.5}$ K	9	(-88.7, 30.1)	T_K	185 K	$117.9^{+88.5}_{-86.1}$ K
		$\log(n(\text{H}_2))$	2.0 cm^{-3}	$4.2^{+1.9}_{-1.7} \text{ cm}^{-3}$			$\log(n(\text{H}_2))$	2.0 cm^{-3}	$2.7^{+2.5}_{-0.5} \text{ cm}^{-3}$
		$\log(N(\text{CO}))$	18.5 cm^{-2}	$19.2^{+1.2}_{-1.0} \text{ cm}^{-2}$			$\log(N(\text{CO}))$	17.5 cm^{-2}	$17.6^{+1.5}_{-1.0} \text{ cm}^{-2}$
		$[^{12}\text{C}]/[^{13}\text{C}]$	40				$[^{12}\text{C}]/[^{13}\text{C}]$	20	
2	(87, -34)	T_K	7 K	$50.8^{+81.8}_{-34.7}$ K	14	(-35.7, -44.1)	T_K	6 K	$7.4^{+24.8}_{-1.6}$ K
		$\log(n(\text{H}_2))$	3.7 cm^{-3}	$2.7^{+1.8}_{-0.5} \text{ cm}^{-3}$			$\log(n(\text{H}_2))$	6.2 cm^{-3}	$5.0^{+1.6}_{-1.9} \text{ cm}^{-3}$
		$\log(N(\text{CO}))$	17.2 cm^{-2}	$17.7^{+0.3}_{-0.4} \text{ cm}^{-2}$			$\log(N(\text{CO}))$	17.7 cm^{-2}	$18.0^{+1.1}_{-0.3} \text{ cm}^{-2}$
		$[^{12}\text{C}]/[^{13}\text{C}]$	30				$[^{12}\text{C}]/[^{13}\text{C}]$	90	
4	(43.9, -17)	T_K	135 K	$128.4^{+78.0}_{-69.4}$ K	15	(-73.1, 64.2)	T_K	25 K	$43.5^{+62}_{-25.3}$ K
		$\log(n(\text{H}_2))$	2.0 cm^{-3}	$2.3^{+0.4}_{-0.2} \text{ cm}^{-3}$			$\log(n(\text{H}_2))$	2.2 cm^{-3}	$2.5^{+1.0}_{-0.4} \text{ cm}^{-3}$
		$\log(N(\text{CO}))$	17.5 cm^{-2}	$17.4^{+0.3}_{-0.4} \text{ cm}^{-2}$			$\log(N(\text{CO}))$	17.7 cm^{-2}	$17.6^{+0.3}_{-0.3} \text{ cm}^{-2}$
		$[^{12}\text{C}]/[^{13}\text{C}]$	20				$[^{12}\text{C}]/[^{13}\text{C}]$	30	
5	(22.4, -9.2)	T_K	65 K	$125.4^{+81.9}_{-76.7}$ K	16	(9.3, 76.8)	T_K	10 K	$40.9^{+100.3}_{-28.1}$ K
		$\log(n(\text{H}_2))$	2.5 cm^{-3}	$2.4^{+1.0}_{-0.3} \text{ cm}^{-3}$			$\log(n(\text{H}_2))$	4.0 cm^{-3}	$4.5^{+1.7}_{-1.8} \text{ cm}^{-3}$
		$\log(N(\text{CO}))$	17.5 cm^{-2}	$17.6^{+0.3}_{-0.3} \text{ cm}^{-2}$			$\log(N(\text{CO}))$	18.2 cm^{-2}	$19.2^{+1.1}_{-0.8} \text{ cm}^{-2}$
		$[^{12}\text{C}]/[^{13}\text{C}]$	20				$[^{12}\text{C}]/[^{13}\text{C}]$	60	
6	(-21.9, 7.2)	T_K	13 K	$91.7^{+97.9}_{-66.2}$ K	17	(-13.4, 103.7)	T_K	5* K	$8.0^{+8.5}_{-2.4}$ K
		$\log(n(\text{H}_2))$	3.2 cm^{-3}	$2.6^{+1.6}_{-0.5} \text{ cm}^{-3}$			$\log(n(\text{H}_2))$	4.2 cm^{-3}	$3.3^{+2.2}_{-1.0} \text{ cm}^{-3}$
		$\log(N(\text{CO}))$	17.2 cm^{-2}	$17.4^{+0.4}_{-0.4} \text{ cm}^{-2}$			$\log(N(\text{CO}))$	17.5 cm^{-2}	$18.0^{+0.6}_{-0.5} \text{ cm}^{-2}$
		$[^{12}\text{C}]/[^{13}\text{C}]$	20				$[^{12}\text{C}]/[^{13}\text{C}]$	90	
7	(-44.4, 14.9)	T_K	160 K	$126.5^{+81.7}_{-72.8}$ K					
		$\log(n(\text{H}_2))$	2.0 cm^{-3}	$2.4^{+0.4}_{-0.3} \text{ cm}^{-3}$					
		$\log(N(\text{CO}))$	17.2 cm^{-2}	$17.1^{+0.5}_{-1.5} \text{ cm}^{-2}$					
		$[^{12}\text{C}]/[^{13}\text{C}]$	20						

Notes: Likelihood results list the median values and 68 per cent (1σ) confidence level. A star (*) indicates a physical parameter lying at the edge of the model grid.

$F_{160\mu\text{m}}$ fluxes. This indicates that the reason for the difference in the UV-brightness between these two groups of positions is not the extinction, but having a different level of star formation activity.

(vii) The UV-bright positions have more diffused gas, indicated by a slightly higher R_{11} ratio found at those positions. Since the UV-bright positions are also hosting many H II regions and brighter at $24\mu\text{m}$ emission, it is natural to expect to have a higher level of star formation activity at those positions, which in turn could make the gas more diffused, compared to the UV-dim positions.

(viii) Both χ^2 and most likely model results indicate that the UV-dim positions mostly have warmer molecular gas with relatively lower $N(\text{CO})$ and $n(\text{H}_2)$, while the UV-bright positions indicate an opposite trend, i.e. colder molecular gas with higher $N(\text{CO})$ and $n(\text{H}_2)$. Additionally, our best model results indicate that the UV-dim positions have abundance ratio ranges from 20 to 40, while the abundance ratio at the UV-bright positions is mostly higher, i.e. ranges from 30 to 90.

ACKNOWLEDGEMENTS

ST would like to thank the anonymous referee for his/her insightful comments and suggestions. ST thanks Timothy A. Davis for very useful discussions. ST thanks Irene San Jose Garcia and Ferhat F. Ozeren for conducting the observation and also thanks to the staff at IRAM 30m telescope for their help with the observations. ST was supported by the Republic of Turkey, Ministry of National Education, The Philip Wetton Graduate Scholarship at Christ Church. ST acknowledge the usage of the HyperLeda database (<http://leda.univ-lyon1.fr>). This research has made use of the NASA/ IPAC Infrared Science Archive, which is operated by the Jet Propulsion Laboratory, California Institute of Technology, under contract with the National Aeronautics and Space Administration.

REFERENCES

Aalto S., Booth R. S., Black J. H., Johansson L. E. B., 1995, A&A,

- 300, 369
- Adler D. S., Knapen J. H., Fanelli M. N., Westpfahl D. J., Wakker B. P., 1999, in *Astronomical Society of the Pacific Conference Series*, Vol. 182, *Galaxy Dynamics - A Rutgers Symposium*, Merritt D. R., Valluri M., Sellwood J. A., eds., p. 227
- Anders E., Grevesse N., 1989, *GeCoA*, 53, 197
- Baan W. A., Henkel C., Loenen A. F., Baudry A., Wiklind T., 2008, *A&A*, 477, 747
- Bayet E., Gerin M., Phillips T. G., Contursi A., 2004, *A&A*, 427, 45
- Bisbas T. G., Wunsch R., Whitworth A. P., Hubber D. A., Walch S., 2011, *ApJ*, 736, 142
- Bolatto A. D., Wolfire M., Leroy A. K., 2013, *ARA&A*, 51, 207
- Calzetti D. et al., 2005, *ApJ*, 633, 871
- Calzetti D., Kinney A. L., Storchi-Bergmann T., 1996, *ApJ*, 458, 132
- Castor J. I., 1970, *MNRAS*, 149, 111
- Crocker A. et al., 2012, *MNRAS*, 421, 1298
- Dale D. A. et al., 2007, *ApJ*, 655, 863
- Dale J. E., Ercolano B., Bonnell I. A., 2012, *MNRAS*, 424, 377
- Dale J. E., Ercolano B., Bonnell I. A., 2013, *MNRAS*, 430, 234
- Dame T. M., Hartmann D., Thaddeus P., 2001, *ApJ*, 547, 792
- de Jong T., Dalgarno A., Chu S.-I., 1975, *ApJ*, 199, 69
- Deharveng L. et al., 2010, *A&A*, 523, A6
- Dobbs C. L. et al., 2014, *Protostars and Planets VI*, 3
- Elmegreen B. G., Lada C. J., 1977, *ApJ*, 214, 725
- Fathi K., Beckman J. E., Zurita A., Relaño M., Knapen J. H., Daigle O., Hernandez O., Carignan C., 2007, *A&A*, 466, 905
- Flores H., Hammer F., Elbaz D., Cesarsky C. J., Liang Y. C., Fadda D., Gruel N., 2004, *A&A*, 415, 885
- Gil de Paz A. et al., 2007, *ApJS*, 173, 185
- Glover S. C. O., Clark P. C., 2012, *MNRAS*, 426, 377
- Goldreich P., Kwan J., 1974, *ApJ*, 189, 441
- Gordon K. D. et al., 2004, *ApJS*, 154, 215
- Hasegawa T., 1997, in *IAU Symposium*, Vol. 170, *IAU Symposium*, Latter W. B., Radford S. J. E., Jewell P. R., Mangum J. G., Bally J., eds., pp. 39–46
- Henkel C., Mauersberger R., 1993, *A&A*, 274, 730
- Henkel C., Mauersberger R., Wiklind T., Huettemeister S., Lemme C., Millar T. J., 1993, *A&A*, 268, L17
- Henkel C., Whiteoak J. B., Mauersberger R., 1994, *A&A*, 284, 17
- Herbert-Fort S., Zaritsky D., Christlein D., Kannappan S. J., 2010, *ApJ*, 715, 902
- Hollenbach D. J., Tielens A. G. G. M., 1999, *Reviews of Modern Physics*, 71, 173
- Israel F. P., 2009a, *A&A*, 493, 525
- Israel F. P., 2009b, *A&A*, 506, 689
- Karachentsev I. D., Karachentseva V. E., Huchtmeier W. K., Makarov D. I., 2004, *AJ*, 127, 2031
- Kennicutt, Jr. R. C. et al., 2003, *PASP*, 115, 928
- Kim J.-G., Kim W.-T., Ostriker E. C., 2018, *ApJ*, 859, 68
- Krips M., Crocker A. F., Bureau M., Combes F., Young L. M., 2010, *MNRAS*, 407, 2261
- Krumholz M. R., Matzner C. D., McKee C. F., 2006, *ApJ*, 653, 361
- Leroy A. K. et al., 2009, *AJ*, 137, 4670
- Makarov D., Prugniel P., Terekhova N., Courtois H., Vauglin I., 2014, *A&A*, 570, A13
- Mao R.-Q., Schulz A., Henkel C., Mauersberger R., Muders D., Dinh-V-Trung, 2010, *ApJ*, 724, 1336
- Markwardt C. B., 2009, in *Astronomical Society of the Pacific Conference Series*, Vol. 411, *Astronomical Data Analysis Software and Systems XVIII*, Bohlender D. A., Durand D., Dowler P., eds., p. 251
- Martín S., Aladro R., Martín-Pintado J., Mauersberger R., 2010, *A&A*, 522, A62
- Matzner C. D., 2002, *ApJ*, 566, 302
- McKee C. F., Ostriker E. C., 2007, *ARA&A*, 45, 565
- Medina S.-N. X., Arthur S. J., Henney W. J., Mellema G., Gazol A., 2014, *MNRAS*, 445, 1797
- Meier D. S., Turner J. L., Hurt R. L., 2008, *ApJ*, 675, 281
- Misiriotis A., Papadakis I. E., Kylafis N. D., Papamastorakis J., 2004, *A&A*, 417, 39
- Paglione T. A. D. et al., 2001, *ApJS*, 135, 183
- Papadopoulos P. P. et al., 2014, *ApJ*, 788, 153
- Sault R. J., Teuben P. J., Wright M. C. H., 1995, in *Astronomical Society of the Pacific Conference Series*, Vol. 77, *Astronomical Data Analysis Software and Systems IV*, Shaw R. A., Payne H. E., Hayes J. J. E., eds., p. 433
- Sobolev V. V., 1960, *Moving envelopes of stars*. Cambridge
- Sun J. et al., 2018, *ApJ*, 860, 172
- Topal S., Bayet E., Bureau M., Davis T. A., Walsh W., 2014, *MNRAS*, 437, 1434
- Topal S., Bureau M., Davis T. A., Krips M., Young L. M., Crocker A. F., 2016, *MNRAS*, 463, 4121
- van der Tak F. F. S., Black J. H., Schöier F. L., Jansen D. J., van Dishoeck E. F., 2007, *A&A*, 468, 627
- van Dishoeck E. F., Black J. H., 1988, *ApJ*, 334, 771
- Wang M., Chin Y.-N., Henkel C., Whiteoak J. B., Cunningham M., 2009, *ApJ*, 690, 580
- Warren B. E. et al., 2010, *ApJ*, 714, 571
- Whitworth A., 1979, *MNRAS*, 186, 59
- Wilson T. L., Rood R., 1994, *ARA&A*, 32, 191

APPENDIX A: SPECTRA

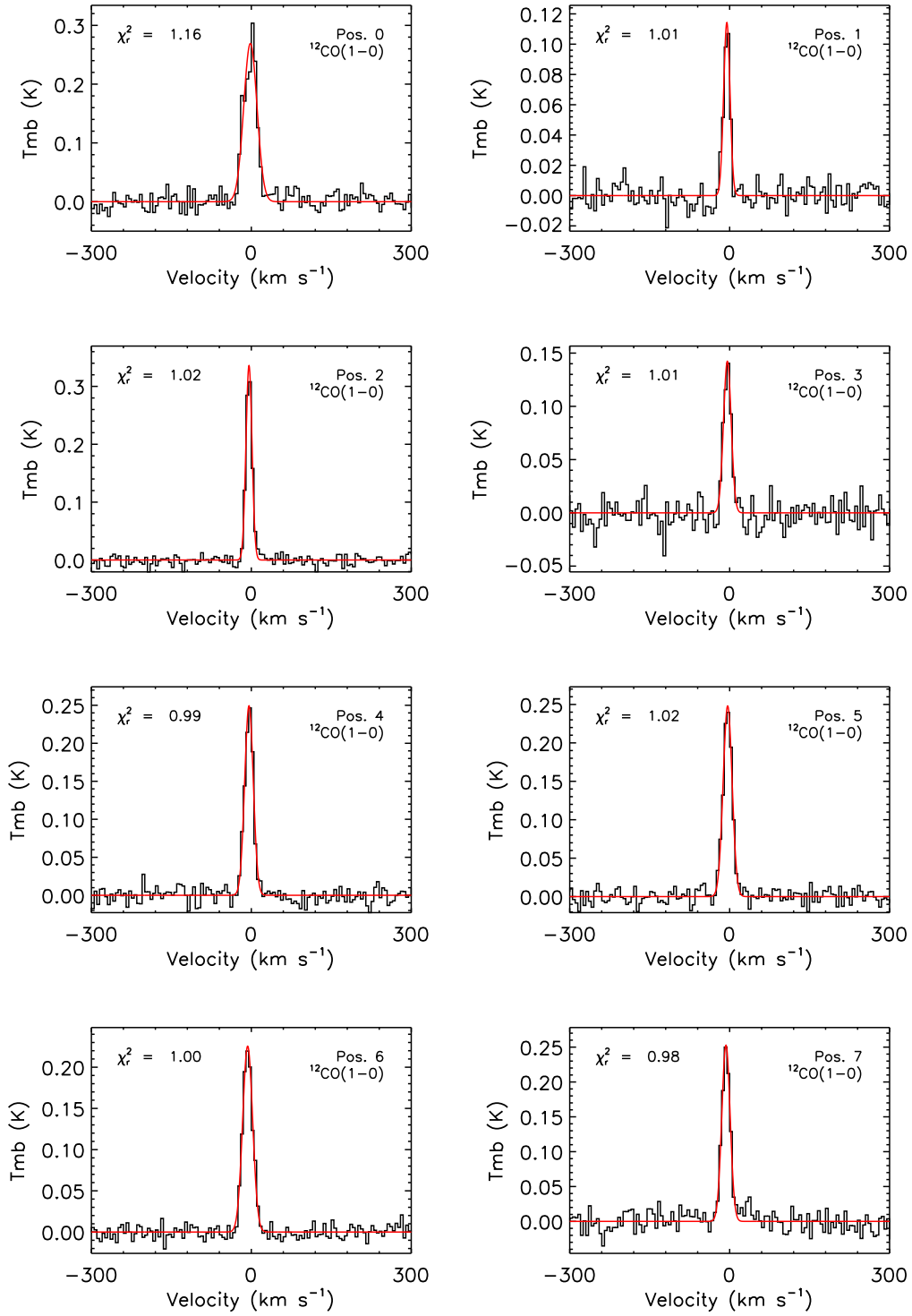


Figure A1. Integrated spectra of CO(1-0) emission observed in the disc of NGC 0628. Gaussian fits are overlaid. The value of χ_r^2 is also shown in each panel.

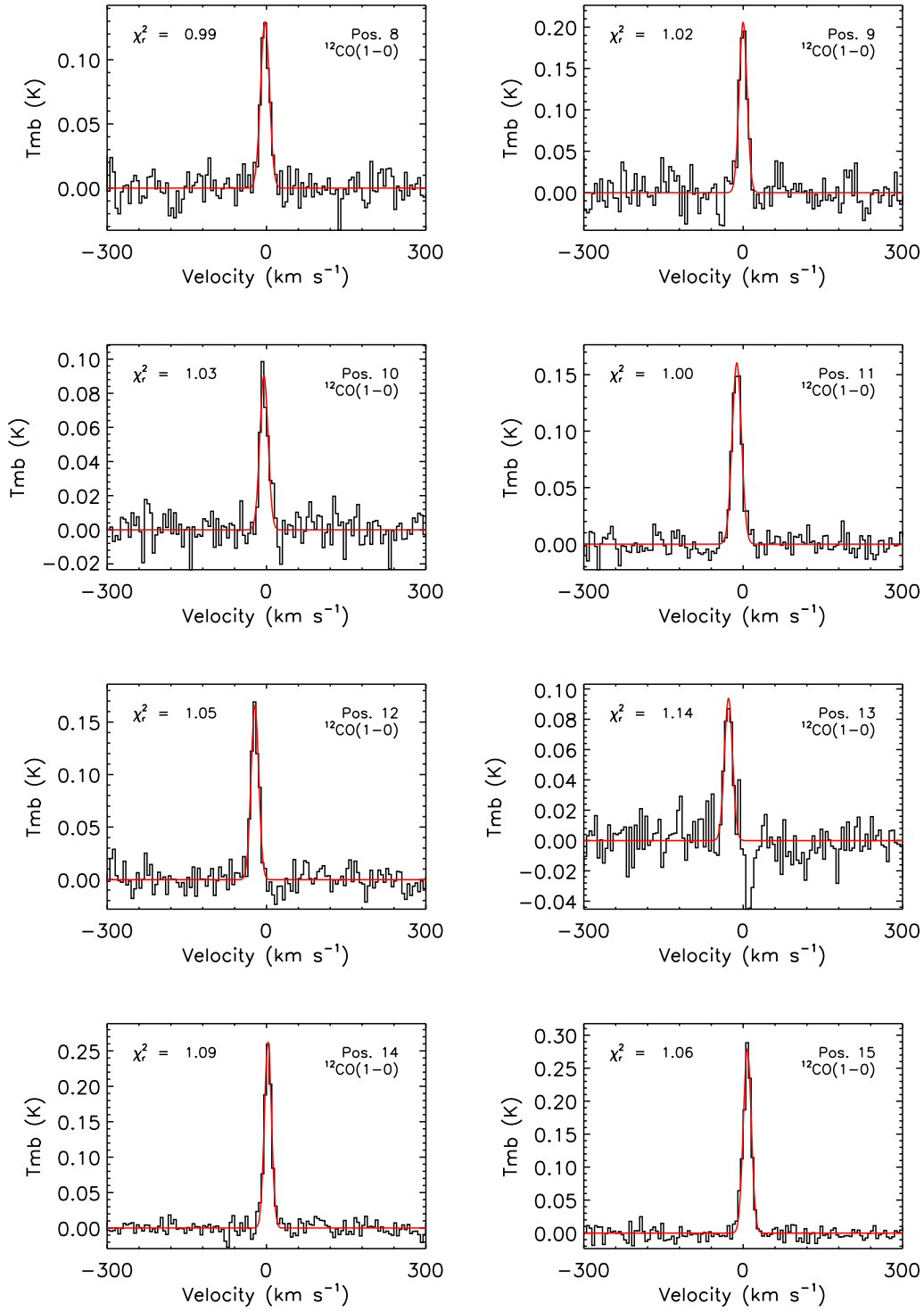


Figure A1. Continued.

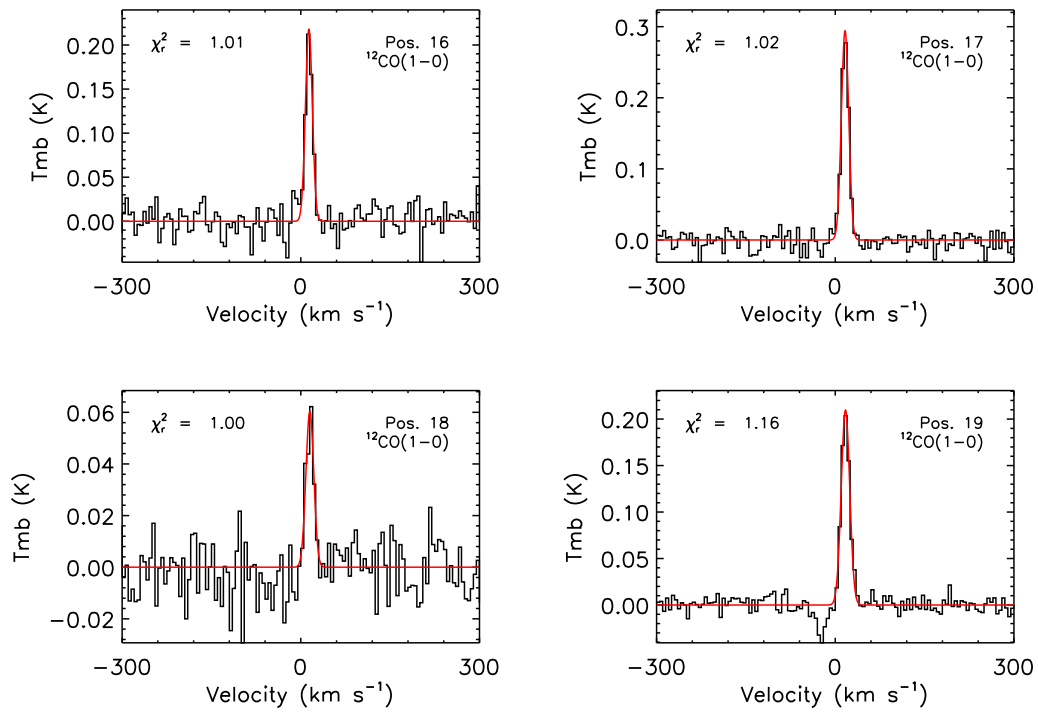


Figure A1. Continued.

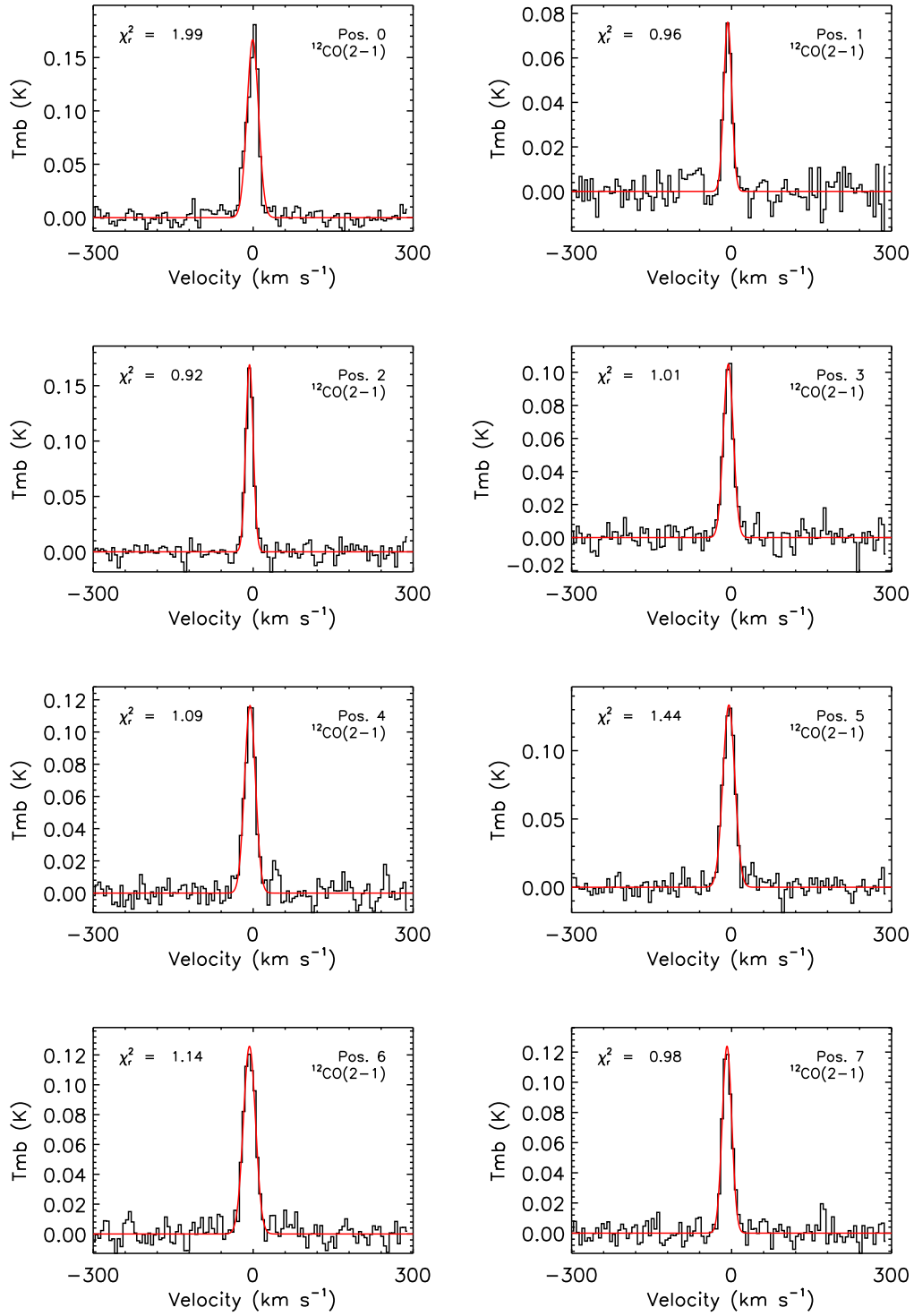


Figure A2. Integrated spectra of the literature CO(2-1) data extracted from the cubes are shown. Gaussian fits are overlaid. The value of χ_r^2 is also shown in each panel.

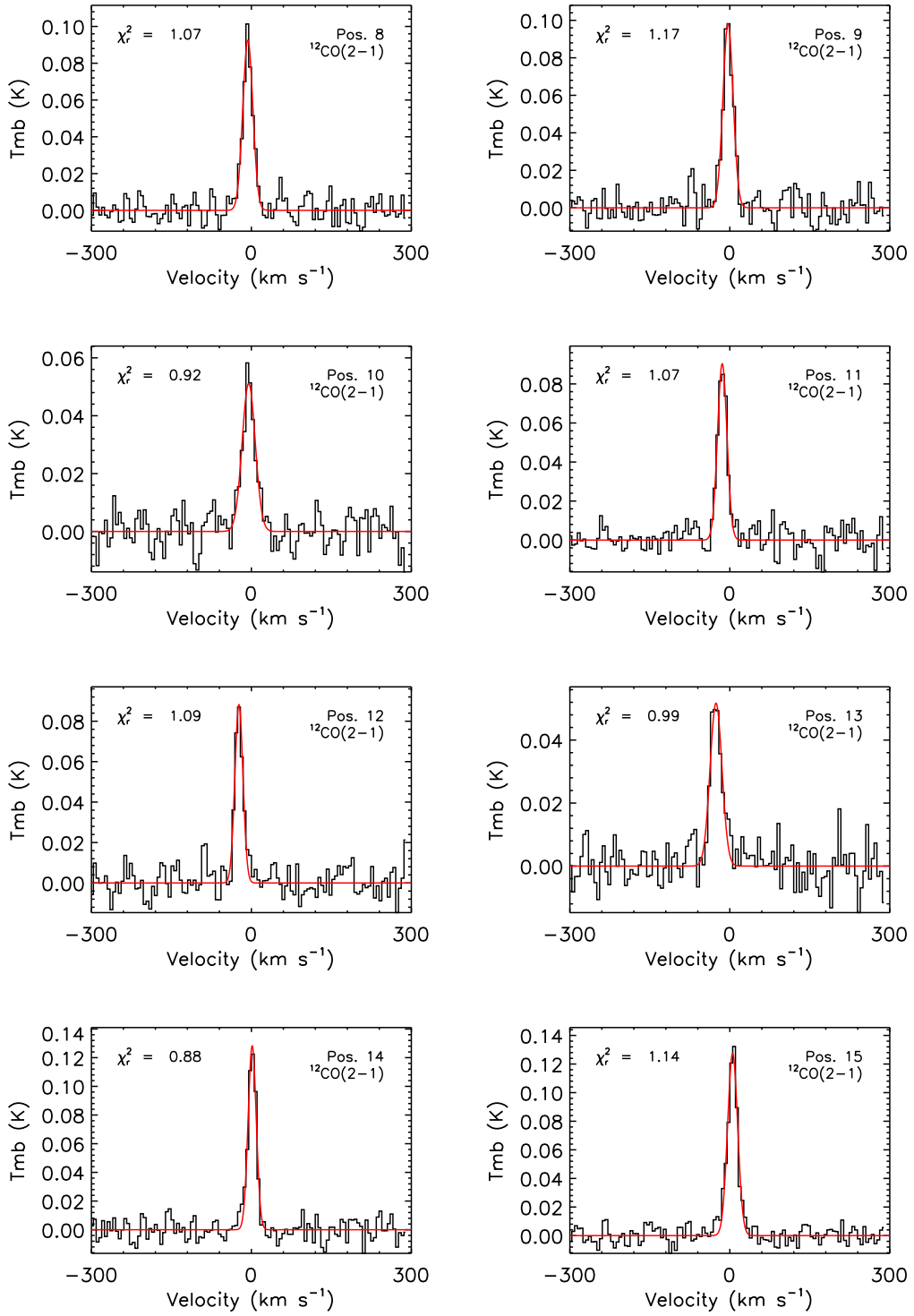


Figure A2. Continued.

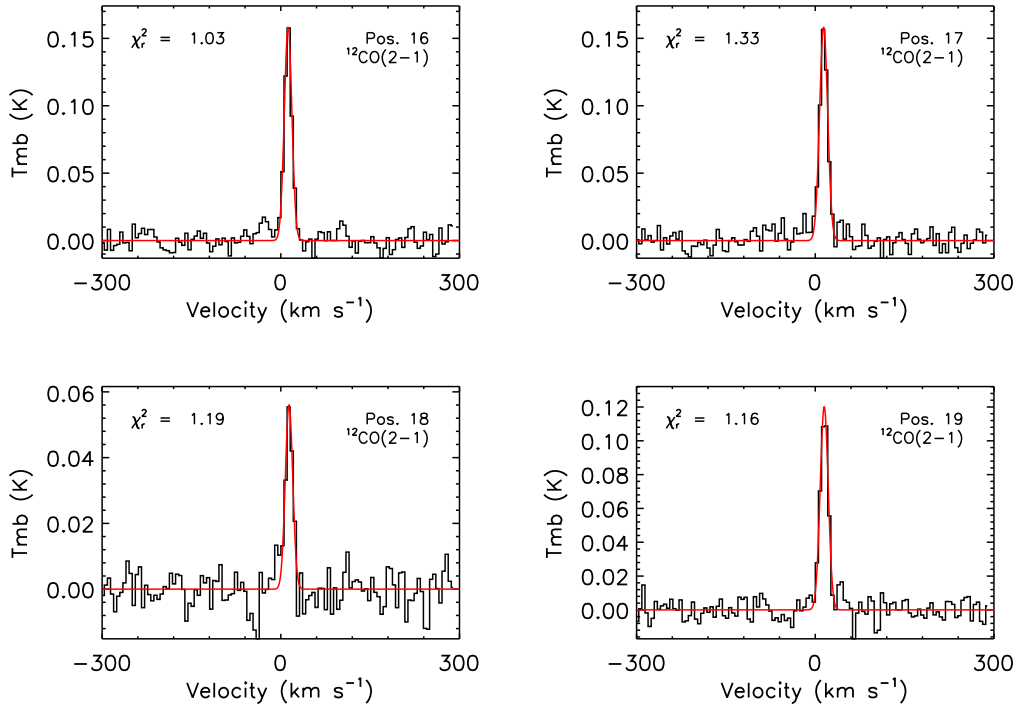


Figure A2. Continued.

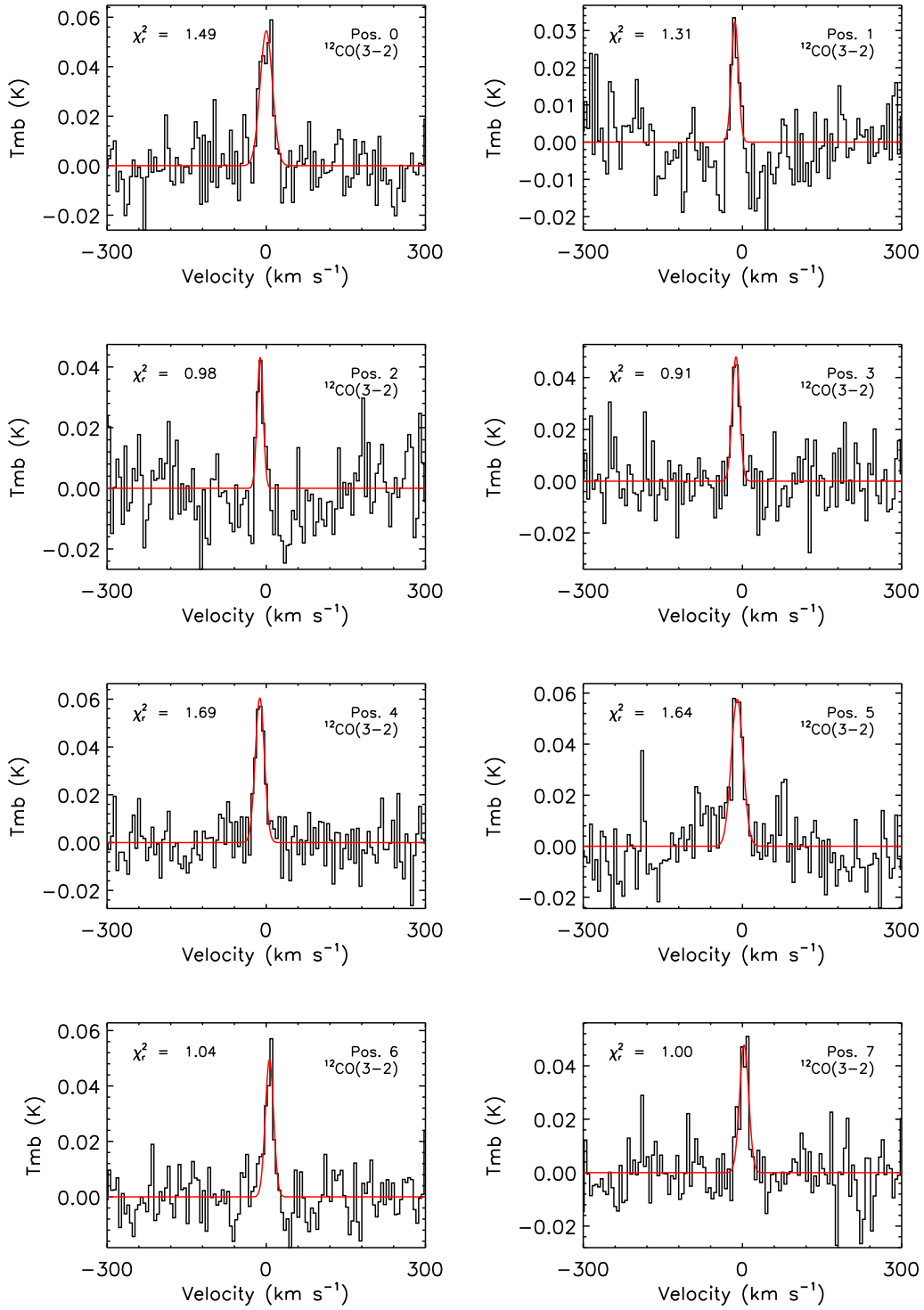


Figure A3. Integrated spectra of the literature CO(3-2) data extracted from the cubes are shown. Gaussian fits are overlaid. The value of χ_r^2 is also shown in each panel.

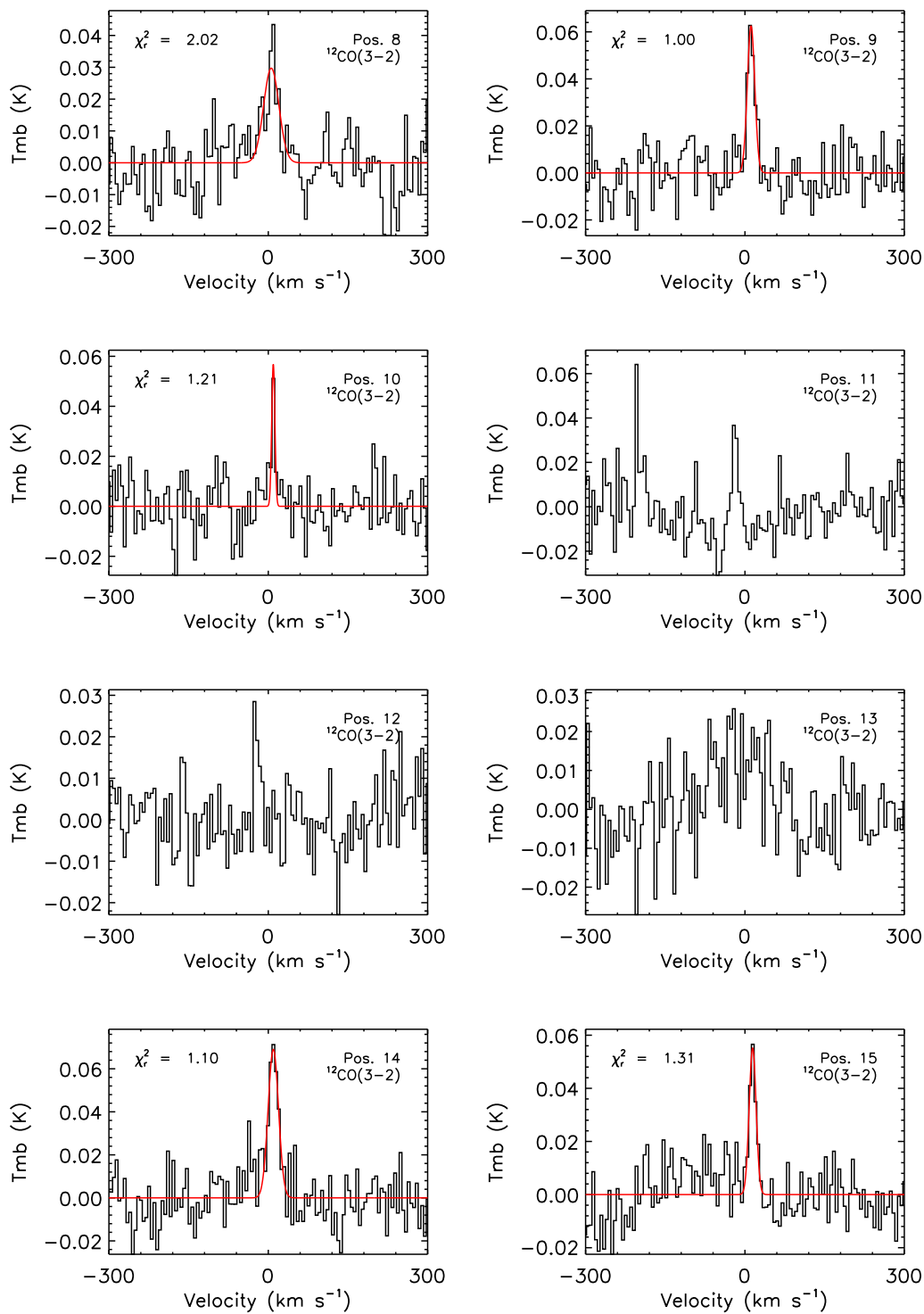


Figure A3. Continued.

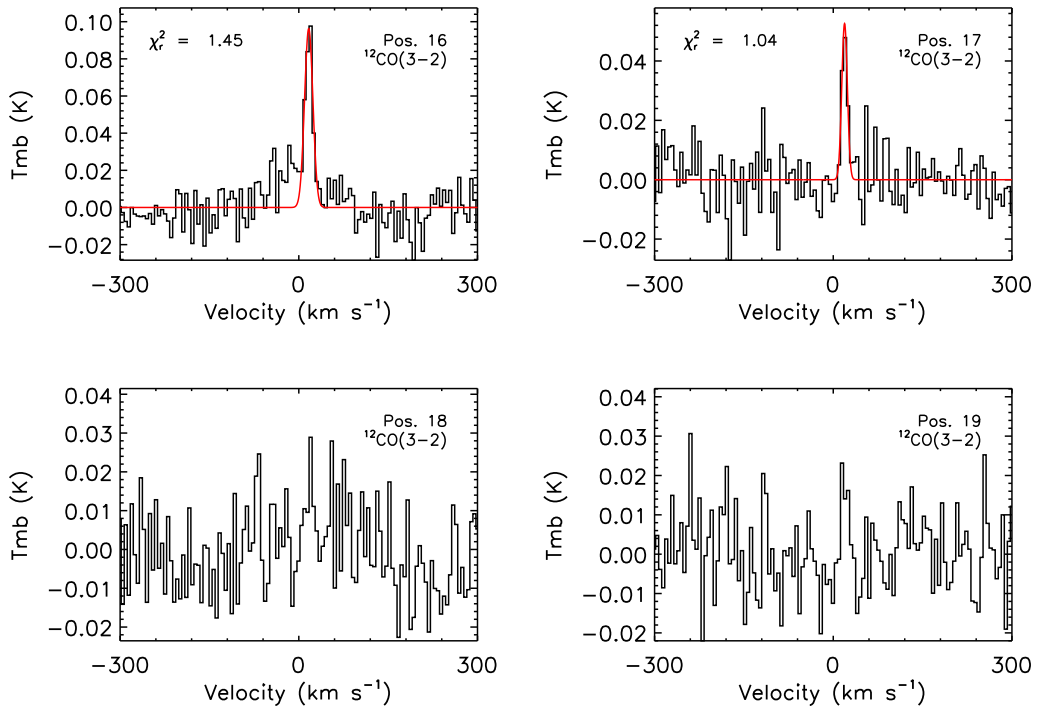


Figure A3. Continued.

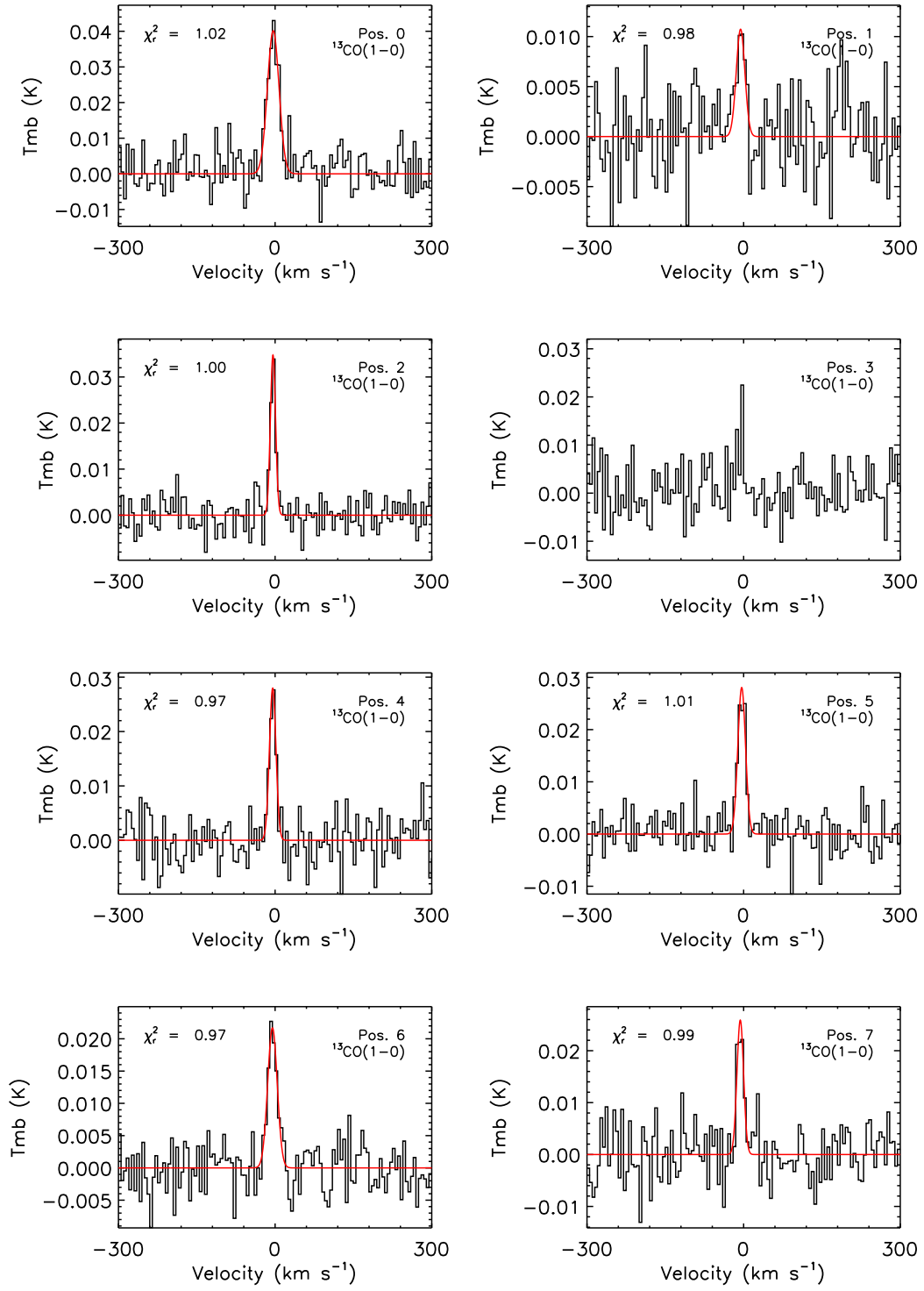


Figure A4. Integrated spectra of $^{13}\text{CO}(1-0)$ emission observed in the disc of NGC 0628. Gaussian fits are overlaid. The value of χ_r^2 is also shown in each panel.

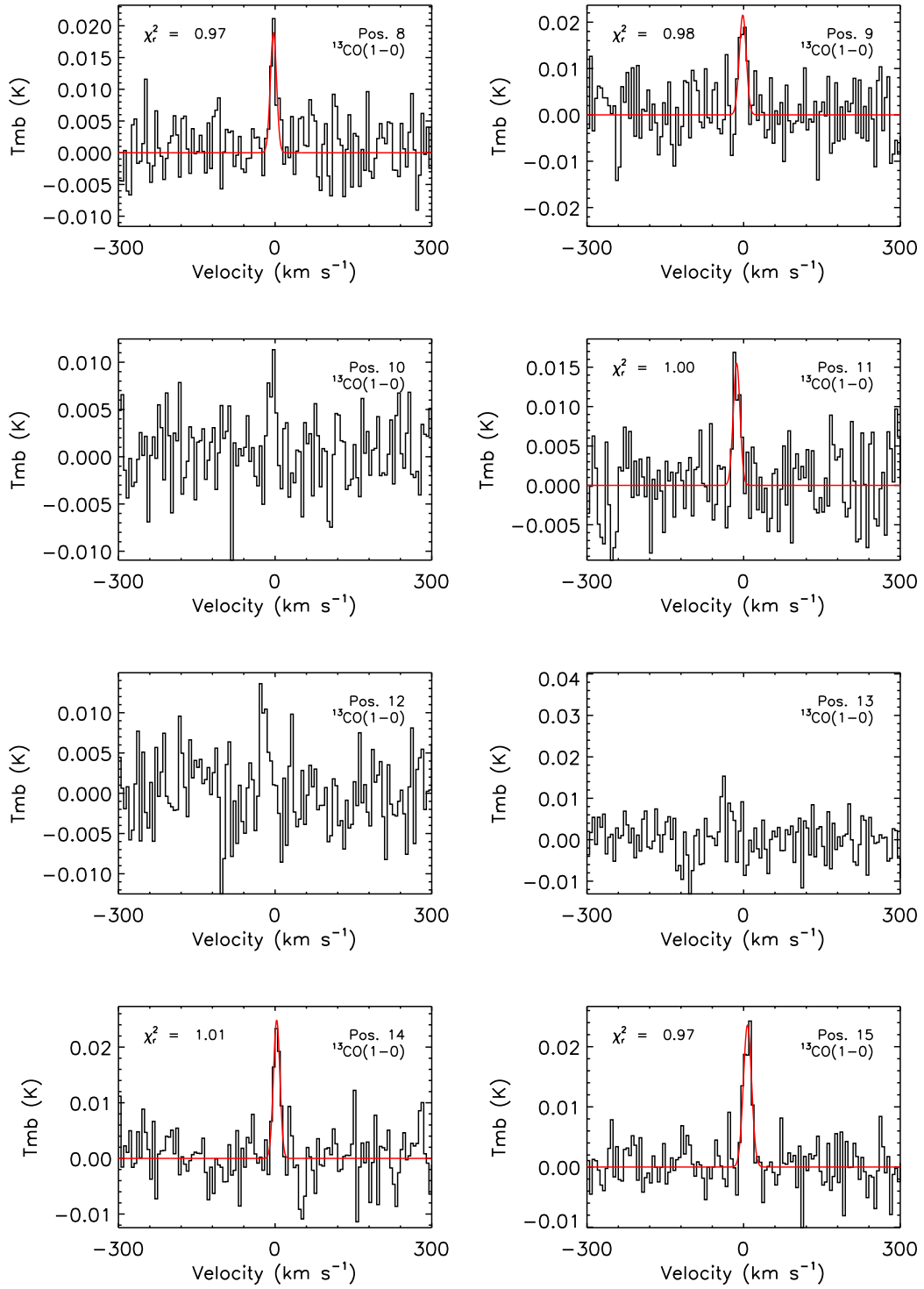


Figure A4. Continued.

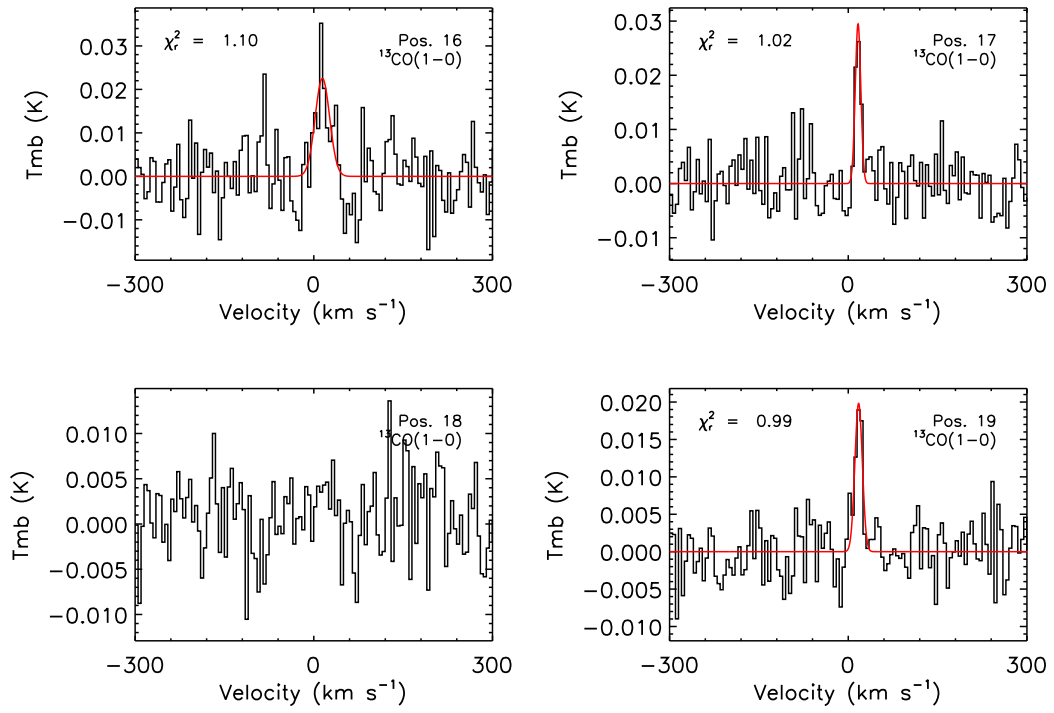


Figure A4. Continued.

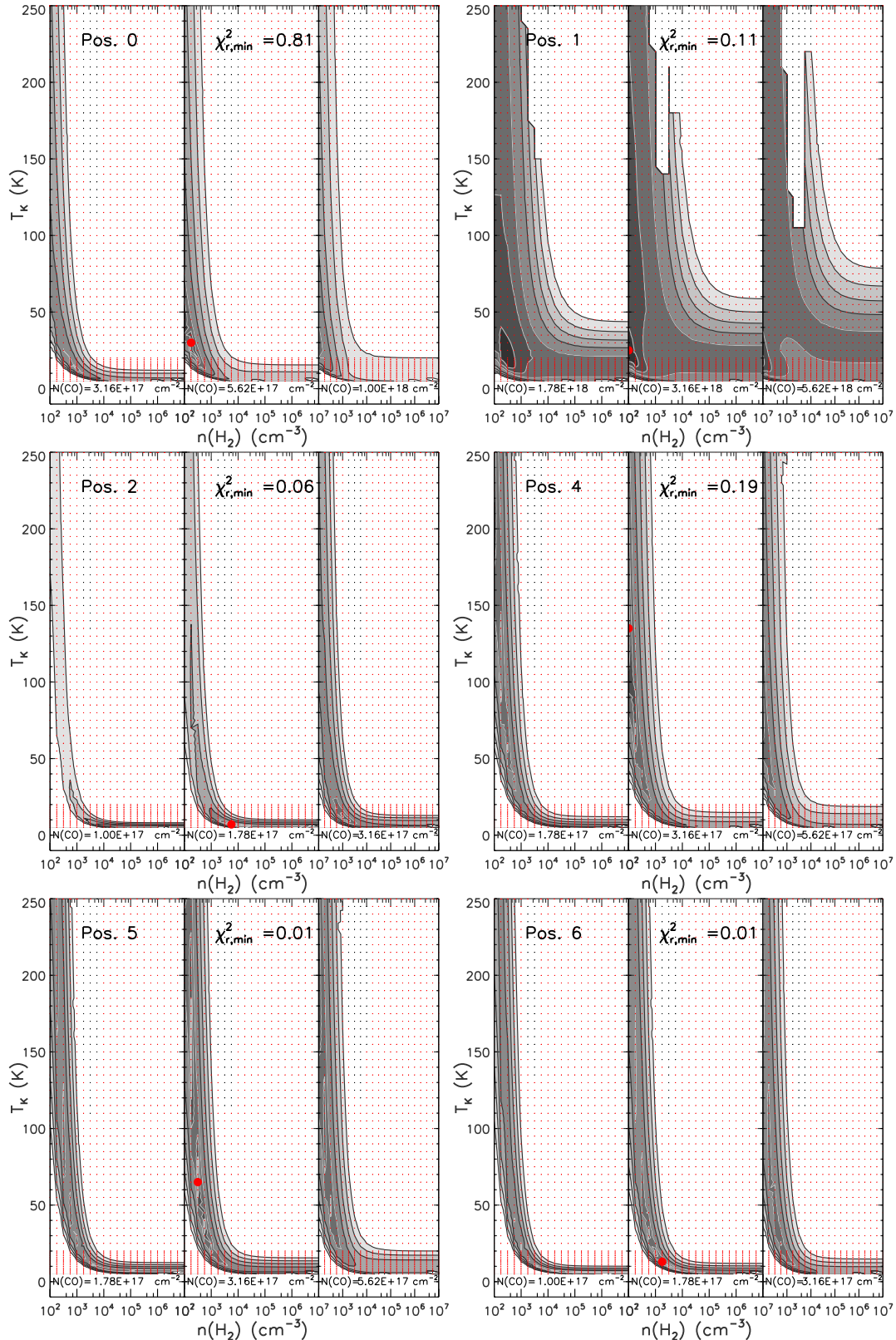


Figure A5. $\Delta\chi_{r,\min}^2 = \chi_r^2 - \chi_{r,\min}^2$ maps for CO gas in NGC 0628 (positions 0, 1, 2, 4, 5, 6). For each position χ_r^2 is shown as a function of T_K and $n(\text{H}_2)$ for three values of CO column density $N(\text{CO})$ centred around the best fit. The values of $N(\text{CO})$ are indicated at the bottom of each panel. As listed in Table 6, the values of $\Delta\chi_{r,\min}^2$ and position numbers are also shown at the top of each panel. The model outputs are indicated by red dots while the best-fitting model are represented by a red filled circle. Black dots represent bad models (e.g., too low opacity; see van der Tak et al. 2007). The contour confidence levels are, 0.2σ (16% probability that the best model is enclosed: the darkest greyscale), 0.5σ (38%), 1σ (68%), 2σ , 3σ , 4σ and 5σ (the lightest greyscale), for 2 degrees of freedom (three line ratios). The values for the level from 0.2σ to 5σ are 0.35, 0.97, 2.30, 6.18, 11.83, 19.33 and 28.74 respectively. The confidence levels from 0.2σ to 1σ are separated by grey lines and those from 2σ to 5σ by black lines.

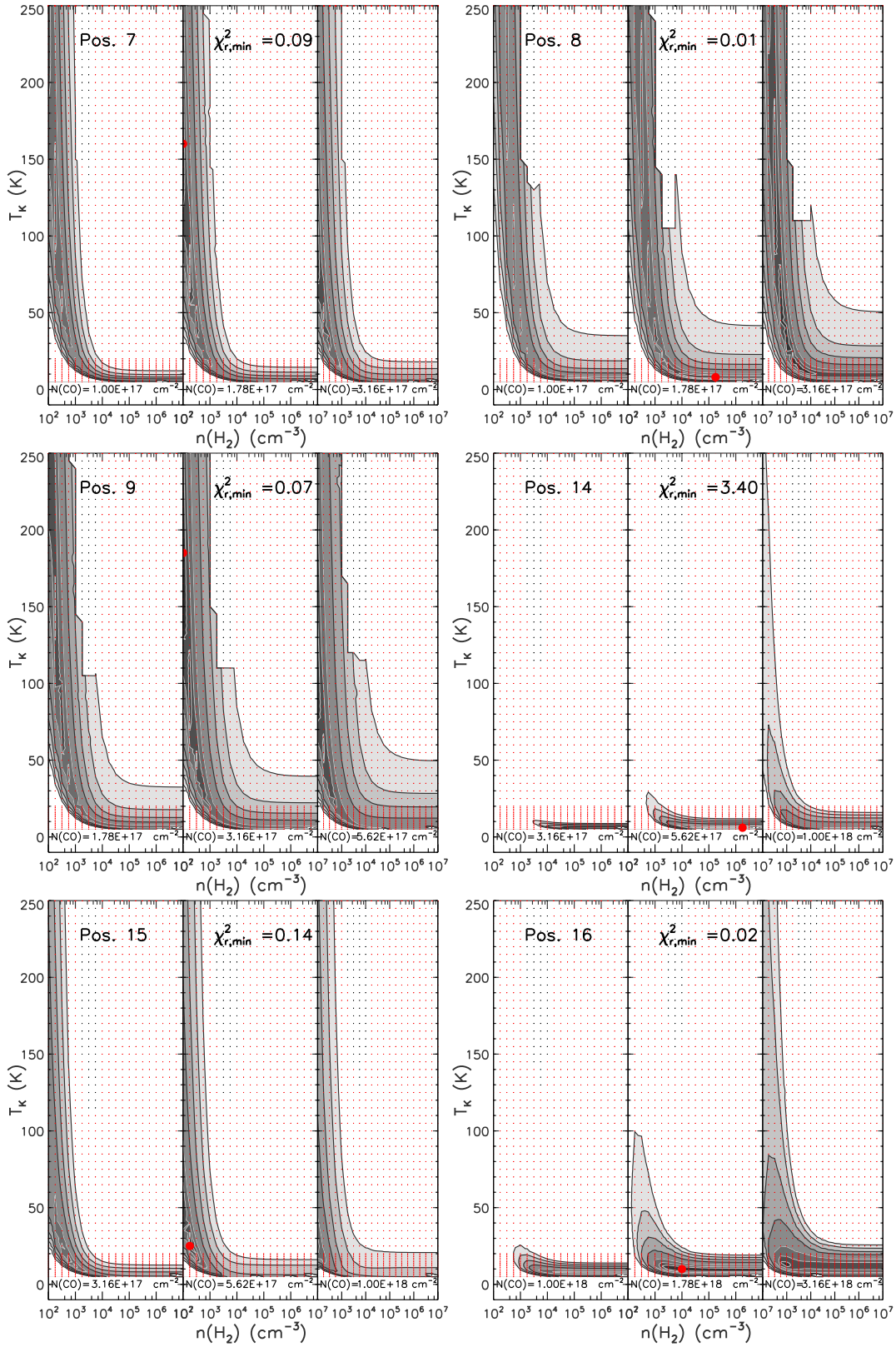


Figure A5. Continued. Same plots as Fig.A5 but for positions 7, 8, 9, 14, 15, and 16.

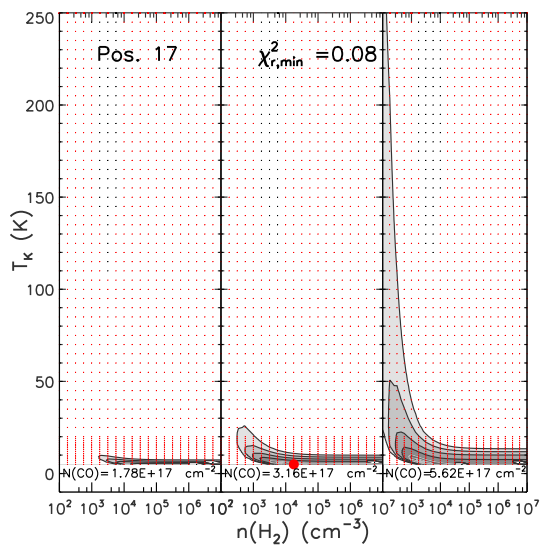


Figure A5. Continued. Same plots as Fig.A5 but for position 17.

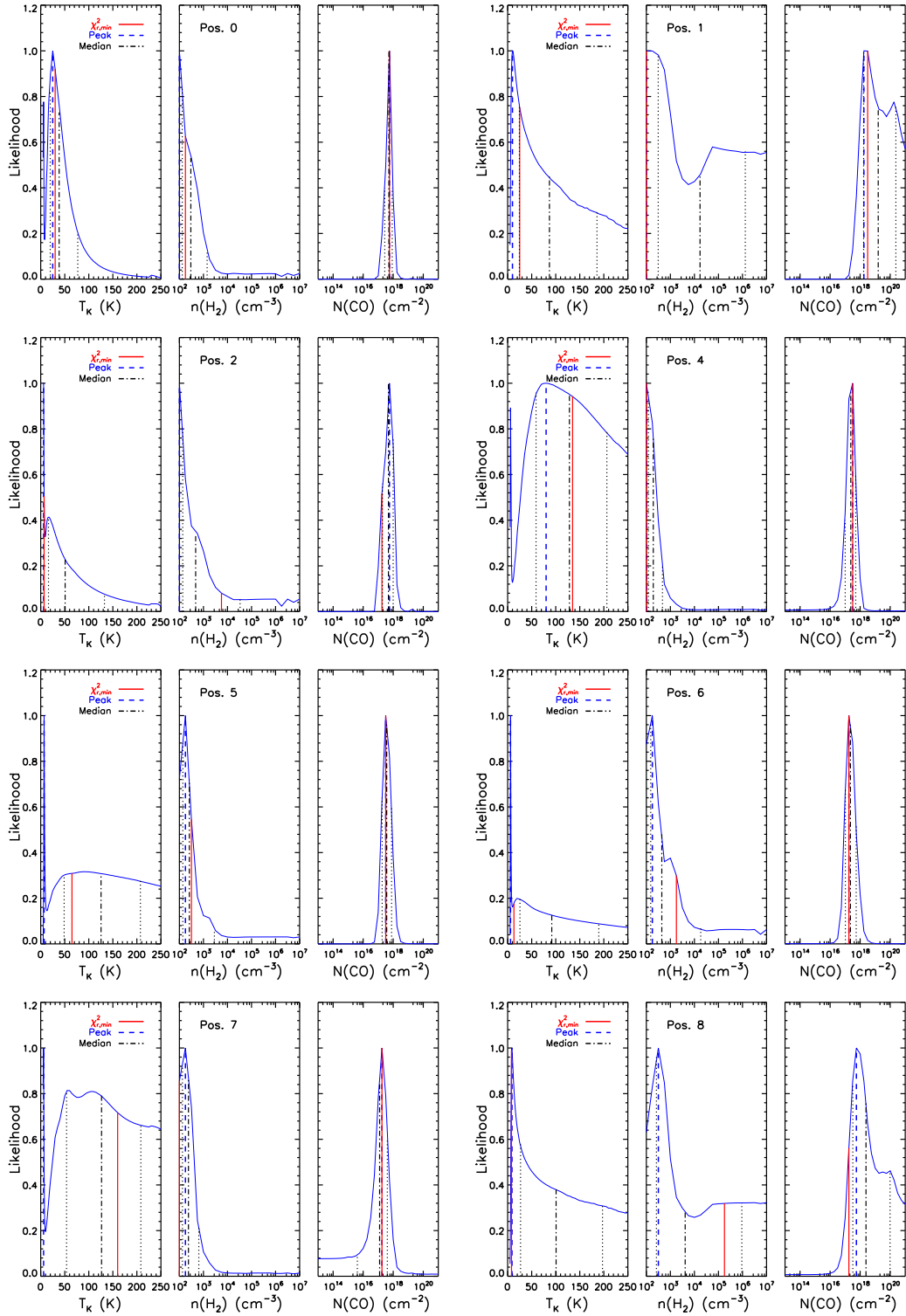


Figure A6. PDF of each model parameter marginalized over the other two, for CO gas in NGC 0628 (positions 0, 1, 2, 4, 5, 6, 7 and 8). In each PDF, the peak (most likely) and median value within the model grid are identified with a dashed blue and dash-dotted black line, respectively. The 68 per cent (1σ) confidence level around the median is indicated by dotted black lines. The best-fitting model in a χ^2 sense is indicated by a solid red line.

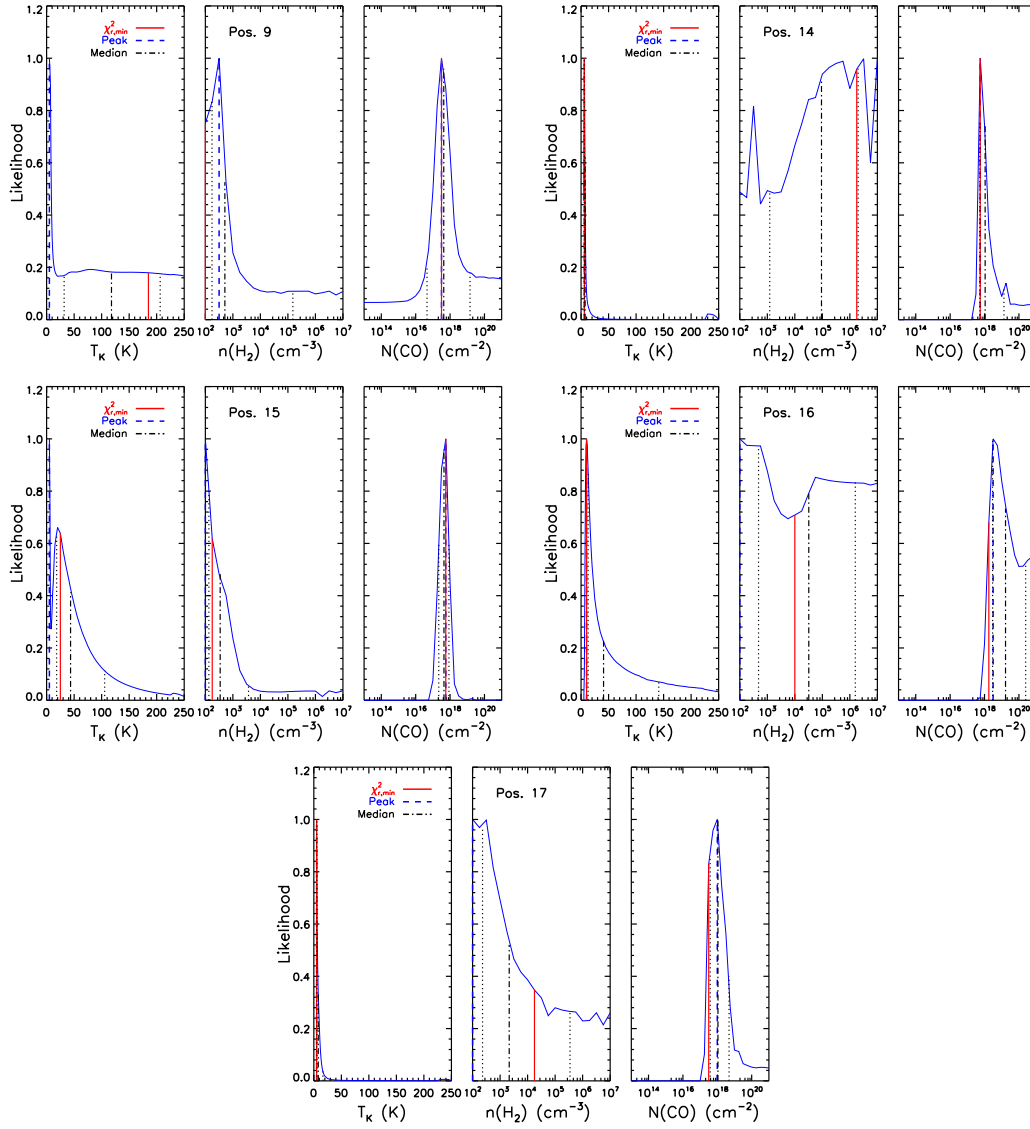


Figure A6. Continued. Same plots as Fig.A6 but for positions 9, 14, 15, 16, and 17.